American Mineralogist, Volume 110, pages 337–363, 2025

Geochemistry and mineralogy of the shale-hosted vanadium Van Property deposit, Mackenzie Mountains, Northwest Territories, Canada

Stefanie M. Brueckner[1,*,†,#], Turner Green[1,‡], Merilie A. Reynolds[2,§], Daniel Gregory[3,‖], and Ricardo Silva[1]

[1]Department of Earth Sciences, University of Manitoba, 125 Dysart Road, Winnipeg, Manitoba R3T 2N2, Canada
[2]Northwest Territories Geological Survey, 4601 52nd Avenue, Yellowknife, Northwest Territories X1A 1K3, Canada
[3]Department of Earth Sciences, University of Toronto, 22 Ursula Franklin Street, Toronto, Ontario M5S 3B1, Canada

Abstract

Shales and mudstones are fine-grained rocks formed in sedimentary basins throughout Earth's history. These lithologies are increasingly important targets for mineral deposit exploration since they can have economic resources of critical minerals, including vanadium (V), an essential component of redox-flux batteries in solar cells. However, many Paleozoic, shale-hosted V deposits are metamorphosed and deformed. This commonly obscures primary features, including V-bearing host phases and the original composition of organic material.

In this study, we present geochemical and mineralogical data from the Paleozoic Van Property deposit, Northwest Territories, Canada, to show that V can be released from organic matter during metamorphism and incorporated in clay phases such as illite. The siliceous argillites at the Van Property host up to 0.69% V_2O_5 and were metamorphosed to (sub-)greenschist facies. Their mineralogy is dominated by quartz with minor graphite, illite, muscovite, pyrite, sphalerite, rutile, and carbonates. Although some illite (i.e., high-V illite) can have up to 13 wt% V_2O_3 and rutile can have up to 4.4 wt% V_2O_3, mass-balance calculations are insufficient to explain V enrichment at the Van Property utilizing only illite and rutile. The third V host is inferred to be carbonaceous matter in which V accumulated syn-deposition on the seafloor. Subsequent metamorphism led to the demetallation of V-bearing geoporphyrins and the release of vanadyl ions (VO^{2+}), some of which were then incorporated into high-V illite and rutile. This process of V enrichment highlights the role of organic matter in scavenging V from superficial reservoirs and the importance of metamorphism on subsequent V release and its incorporation into inorganic phases. The geochemistry of siliceous, V-rich argillites at the Van Property is also compared to other V-enriched shale and mudstone deposits, highlighting the diversity of shale-hosted V deposits and emphasizing the need for further research to close the knowledge gaps related to variations in composition, mineralogy, and V enrichment processes.

Keywords: Vanadium, shale-hosted V deposits, Van Property, illite, carbonaceous matter, V-bearing geoporphyrins, vanadyl ion, metamorphism, Critical Minerals for a Sustainable Future

Introduction

The demand for critical metals has significantly increased over the last decade due to advancements in the environmental needs of low-carbon energy technologies [e.g., the development of electric car batteries for mass production, batteries for energy storage (Schulz et al. 2017; Jowitt et al. 2018; Simandl et al. 2023)]. Many governments and agencies have published lists of critical metals (Schulz et al. 2017; European Commission 2020; Natural Resources Canada 2020; Su and Hu 2022; USGS 2022), highlighting both the economic importance and vulnerability in the supply chain of critical metals. Among these critical metals, the element vanadium (V) has yet to be in the spotlight of both research and economy despite its increasing importance, especially in the redox-flux batteries used in solar cells for energy storage (Kelley et al. 2017; Jowitt et al. 2018; Elbokl 2022; Simandl and Paradis 2022).

Most of the global V production is currently mined as a by-product from magmatic vanadiferous titanomagnetite deposits [e.g., Bushveld complex: Maier et al. (2012), Viljoen (2016), Boni et al. (2023); Lac Dore, Quebec, Canada: Fischer (1975), Longridge and Martinez (2020); Panzhihua layered intrusion, China: Zhou et al. (2005)] and to a lesser extent from sedimentary sandstone-hosted deposits that are enriched in other critical elements such as uranium [e.g., Colorado Plateau; Slick Rock district, Colorado: Shawe (2011); Pandora deposit, Utah: Fischer (1968)]. The third important type of V deposit is the shale-hosted V deposits [e.g., Green Giant, Madagascar: Di Cecco et al. (2018); several deposits in Mozambique: Boni et al. (2023) and references therein]; however, no currently active shale deposits are being mined for V, despite the relatively large abundance of black shales and mudstones on and near the surface. The reasons for this are

* Present address: Harquail School of Earth Sciences, Laurentian University, 935 Ramsey Lake Rd., Sudbury, ON P3E 2C6, Canada. Corresponding author E-mail: sbrueckner@laurentian.ca ORCID https://orcid.org/0000-0002-0702-1037
† Special collection papers can be found online at our website in the Special Collection section.
‡ Present address: Department of Geology, Lakehead University, 955 Oliver Rd., Thunder Bay, ON P7B 5E1, Canada.
§ ORCID https://orcid.org/0000-0003-3442-2597
‖ ORCID https://orcid.org/0000-0001-8901-3913

economic (e.g., lower average V content compared to titano-magneto-ferrous deposits and relatively low V prices currently) and geological, such as the lack of exploration in sedimentary basins specifically for V, ignorance of V-enrichment processes in black shales, and beneficiation of black shales at profitable recovery rates for V (Vitolo et al. 2000; Li et al. 2021; Simandl and Paradis 2022). Closing the geological knowledge gap by developing a holistic deposit model that addresses both the mineralogy of shale-hosted V deposits and their formation is important to support exploration efforts and increase chances of success.

This study focuses on the metamorphosed Van Property in the Mackenzie Mountains, Northwest Territories, and utilizes lithogeochemistry and mineral compositions to describe how host lithology and mineralogy impact V enrichment and the role that metamorphism plays in epigenetic V remobilization. Detailed scanning electron microscopy, electron microprobe analyses, and X-ray diffraction focused on V-bearing phases highlight that the enrichment of V occurs syngenetically with metamorphic alteration of the V host phases. The chemical composition of the Van Property is compared to other Paleozoic shale-hosted V deposits, highlighting variations in host lithology, geochemistry, and V-hosting mineralogy among this deposit type. The results of this study contribute to filling knowledge gaps within this yet understudied deposit class and provide a better understanding of the compositional and mineralogical variety among shale-hosted V deposits, which has important implications for V-enrichment processes. Hence, results from this study have direct impacts on our understanding of ore-forming processes in shale-hosted V deposits and their exploration.

Geological setting

Regional setting

The Mackenzie Mountains comprise the western part of the Mackenzie Platform and the eastern part of the Selwyn Mountains; they are part of Ancestral North America, located on the western part of Laurentia (Nelson et al. 2013). There, they form the most northeastern extension of the Cordillera (Gordey and Roots 2011; Ootes et al. 2013; Fig. 1). Stratigraphically, rocks from the Neo-Proterozoic to the Cretaceous are preserved in the

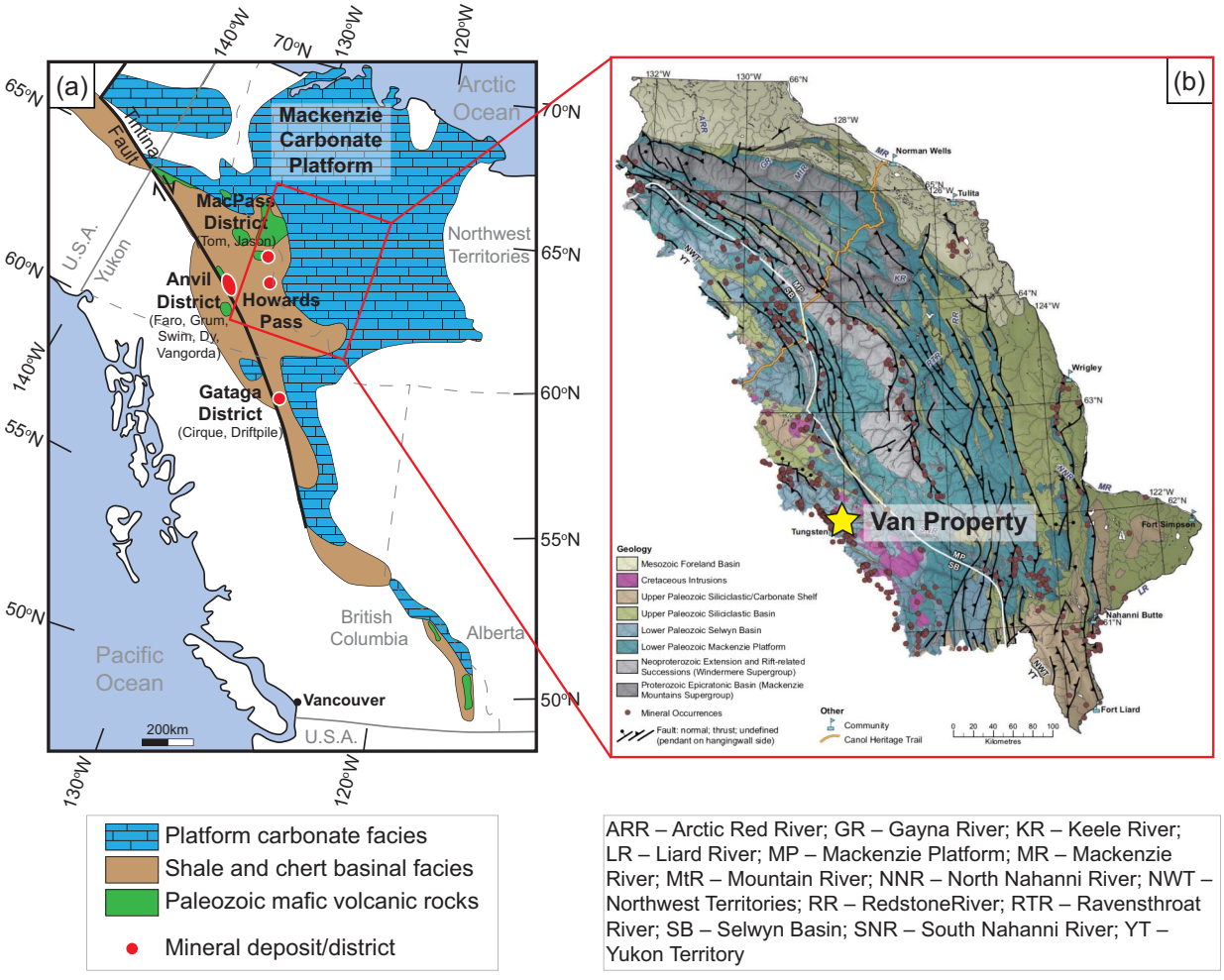

Figure 1. Simplified geologic maps of (**a**) the Selwyn Basin with Mackenzie carbonate platform and Mackenzie Mountains, and major mineral deposits (Goodfellow and Lydon 2007; Slack et al. 2016); and (**b**) the Mackenzie Mountains (Ootes et al. 2013 and references therein) with the Van Property (yellow star) of which a detailed geologic map is provided in Figure 2.

Mackenzie Mountains. The Neo-Proterozoic strata include the older Mackenzie Mountains Supergroup (<1.05 and >0.78 Ga; Turner 2010; Gordey and Roots 2011; Long and Turner 2012) and the younger Windermere Supergroup (≈755 to 550 Ma; Narbonne and Aitken 1995; Gordey and Roots 2011; Ootes et al. 2013). The former consists of carbonate and clastic strata of 4 to 6 km thickness formed in deltaic, fluvial, and shelf settings of a large epicratonic basin (Rainbird et al. 1996; Long et al. 2008; Turner and Long 2008). After the breakup of Rodinia, sedimentation on Laurentia's western margin started as early as 755 Ma, forming the carbonate, shallow to deep-marine clastic, and glacially influenced clastic strata of the Windermere Supergroup, which is 5 to 7 km thick and deposited in a rift-related setting (Narbonne and Aitken 1995; Gordey and Roots 2011; Ootes et al. 2013). Sedimentation continued into the Paleozoic with shallow-water carbonates deposited on the Mackenzie Platform to the northeast and coeval deeper-water marine strata deposited in the Selwyn Basin to the southwest (Fig. 1a and 1b). Although no structurally controlled boundary on the platform margins is evident on the surface, deeper crustal features may have contributed to subsidence and the different depositional environments (Cecile 1982; Gordey and Roots 2011).

Paleozoic strata of the carbonate platform include basal Ediacaran to Cambrian shallow-marine to fluvial quartz sandstone and minor carbonate rocks that are overlain by Cambrian to Devonian formations dominated by dolostone with minor limestone and siliciclastic rocks; open-marine Devonian carbonate rocks complete the succession (e.g., Gordey and Roots 2011; Turner et al. 2011; Ootes et al. 2013). Coeval Paleozoic strata of the Selwyn Basin are dominated by fine-grained deep-water marine sediments. The simplified stratigraphy of the south-central Selwyn Basin is shown in Figure 2. The Vampire, Sekwi, and Rabbitkettle formations, and the Road River Group are all exposed in the study area (Fig. 3); more detailed descriptions of these units are provided below.

During the Late Devonian, depositional regimes changed in the Mackenzie Mountains siliciclastic dominated the strata making up the Lower Devonian to Middle Mississippian Earn Group. Siliceous mudstones and carbonaceous cherts of this unit are present both in the south-central Selwyn Basin and study area (Figs. 2 and 3) and received their detritus from western sources that included elevated fault blocks of older Selwyn Basin strata (Gordey 1988; Gorey and Anderson 1993). Although sedimentation continued during the Early Carboniferous and Permian, the stratigraphic record is fragmented throughout the Mackenzie Mountains and absent in the study area. Cretaceous shale and sandstone, pebble and cobble conglomerate, and localized coal streams are restricted to the Mackenzie Platform in the northern Mackenzie Mountains (Fig. 1b).

Mid-Cretaceous plutonism is common throughout the Mackenzie Mountains (Gordey and Roots 2011; Ootes et al. 2013). However, plutons intruded in Selwyn Basin strata are typically of Jurassic age and are composed of alkaline, calc-alkaline, and two-mica granite (Woodsworth et al. 1991; Gordey and Roots 2011).

Strata of the Selwyn Basin underwent low-grade metamorphism of sub-greenschist to greenschist facies during the Jurassic in relation to the formation of the Cordillera in the west (Gordey and Roots 2011). In the aureoles of Cretaceous plutons, contact metamorphism is reported throughout the Mackenzie Mountains (Gordey and Anderson 1993). Dominant faults in the Mackenzie Mountains are northwest-southeast trending (Fig. 1b) and are either syn-sedimentary extensional faults developed dominantly during the Paleozoic (Aitken and Cook 1974; Eisbacher 1981; Turner and Long 2008; Pyle and Jones 2009; Gordey et al. 2011) or Cretaceous-Tertiary folds and thrust faults (Morris and Nesbitt 1998; Mair et al. 2006; Pyle and Jones 2009; Gordey and Roots 2011).

Mineralization is common in the Mackenzie Platform and Selwyn Basin strata of the Mackenzie Mountains (Fig. 1b) with over 300 known mineral occurrences (Ootes et al. 2013). Most of these occurrences are clastic-dominated (a.k.a., sedimentary exhalative) Zn-Pb deposits in the Selwyn Basin (e.g., Howard's Pass) or carbonate-hosted Zn-Pb deposits (e.g., Prairie Creek, Gayna River) in the Mackenzie Platform; these deposits formed during the Paleozoic (Fig. 2; (Ootes et al. 2013). Tungsten-skarn deposits (e.g., Cantung and Mactung deposits) related to Cretaceous intrusions occur in the Selwyn Basin close to the Van Property study area (Fig. 1b).

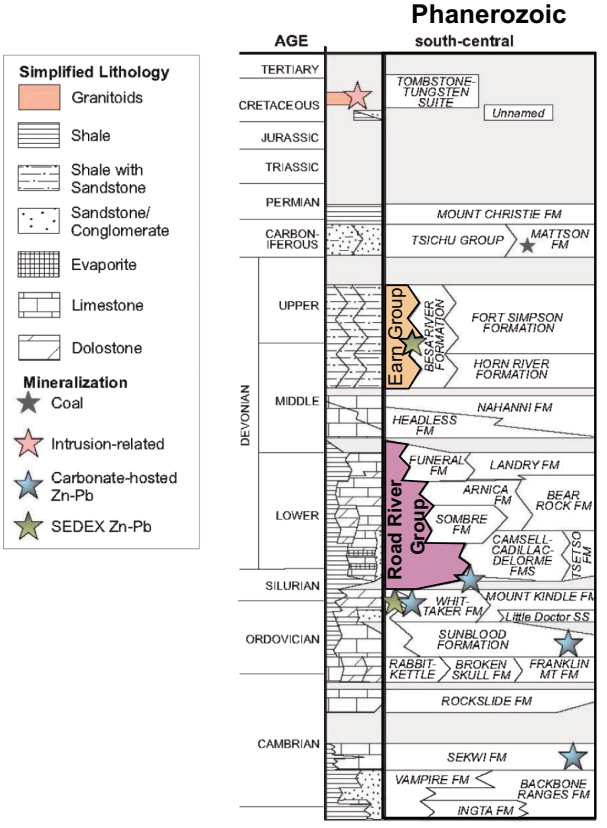

Figure 2. Simplified Phanerozoic stratigraphy of the Mackenzie and eastern Selwyn Mountains with mineral occurrences after Ootes et al. (2013) (modified and simplified after Dixon 1999; Dewing et al. 2006; Pyle and Jones 2009; Martel et al. 2011 and references therein). Note: Gray shade represents regions where no rock record is preserved. Highlighted Earn and Road River Group were sampled for this study.

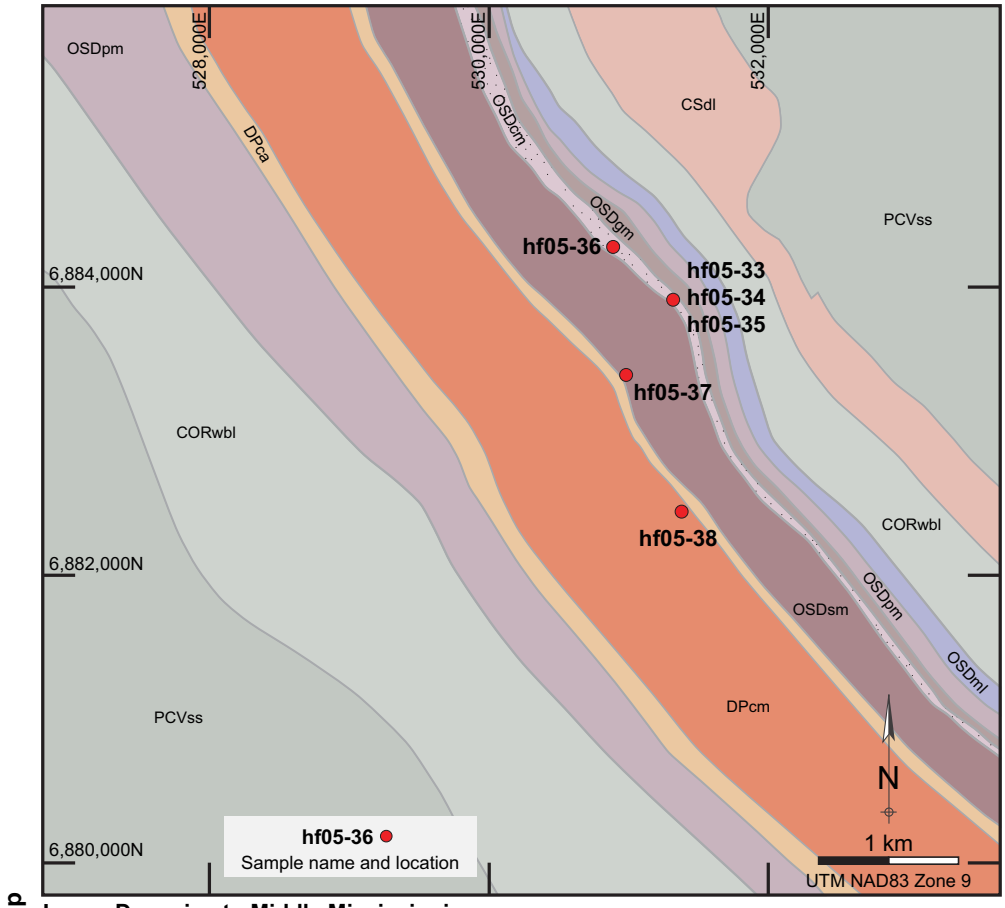

Earn Group

Lower Devonian to Middle Mississippian

DPcm — **Prevost Formation:** Brown weathering, laminated carbonaceous mudstone with minor black chert and baritic mudstone

DPca — **Portrait Lake Formation:** Thin bedded carbonaceous chert with minor intercalated siliceous mudstone; large (1-3m) limestone concretions

Road River Group

Lower Ordovician to Devonian: Duo Lake Formation (OSD)

OSDsm — **Upper Siliceous Mudstone Member:** Thin bedded, carbonaceous, siliceous mudstone with abundant black, coarse crystalline, fetid limestone concretions up to 3 m; distinct graptolite (*Monograptus*) zone at top

OSDcm — **Lower Cherty Mudstone Member:** Thick bedded, blocky fracturing siliceous mudstone

OSDgm — **Calcareous Mudstone Member:** Thin bedded, laminated, calcareous, carbonaceous, graptolitic mudstone

OSDpm — **Siliceous Mudstone Member:** Pyritic, siliceous mudstone

OSDml — **Transition Member:** Laminated mudstone with minor intercalated, trilobite-bearing limestone

Upper Cambrian and Lower Ordovician

CORwbl — **Rabbitkettle Formation:** Interbedded grey weathering platy limestone and light brown weathering silty dolomite

Lower Cambrian

CSdl — **Sekwi Formation:** Orange weathering dolomite and grey weathering limestone

Upper Proterozoic and Lower Cambrian

PCVss — **Vampire Formation:** Grey to brown siltstone and green phyllite with local limestone interbeds

Figure 3. Detailed geological map of the Van Property with sample locations. Descriptions of stratigraphic units are from Carne and Gish (1999). Map modified after Flavelle (2013). A summary of samples is provided in Table 1.

Local geological setting

The Van Property is located in the Flat Lakes area, southwestern Northwest Territories (Fig. 1). Stratigraphically, the Van Property occurs in Paleozoic strata of the Selwyn Basin, which form a large-scale, northwest-trending, upright syncline with near vertical limbs; no large-scale regional faults are observed (Carne and Gish 1999). At the Van Property, Upper Proterozoic to Middle Mississippian strata occur (Fig. 2), which are summarized here after Carne and Gish (1999) and Flavelle (2013).

The oldest unit, Upper Proterozoic to Lower Cambrian Vampire Formation, comprises gray to brown siltstone and green phyllite with local limestone interbeds and is conformably overlain by the Lower Cambrian Sekwi Formation. At the Van Property, the latter only occurs in the northeast (Fig. 2) and consists of dolostone and distinctively orange-weathered limestone. Both lithologies are common throughout the Selwyn Basin, with reported thicknesses of 390 and 700 m for the Vampire and Sekwi formations, respectively (Gordey and Roots 2011). However, the thickness of each formation is not reported from the Van Property. The Upper Cambrian to Lower Ordovician Rabbitkettle Formation sharply overlays the Sekwi Formation and is the most visually distinctive unit in the study area due to the differential weathering of more competent fine-grained dolomite beds with less-weather-resistant, silty limestone lenses. At the Van Property, this unit is 65 to 75 m thick, much less than the reported thickness of 435 to 840 m in other parts of the Selwyn Basin (Gordey and Roots 2011). Carne and Gish (1999) interpreted the sharp transition between the Rabbitkettle Formation and overlying Road River Group as an unconformable or a disconformable contact. None of the afore-described units (Vampire, Sekwi, Rabbitkettle formations) show mineralization, including V, in the study area.

The Lower Ordovician to Devonian Road River Group is widespread in the Selwyn Basin, although its nomenclature is problematic (Cecile 1982; Gordey and Roots 2011; Turner et al. 2011). At the Van Property, the Road River Group is represented by the shale-dominated, recessive Duo Lake Formation (OSD). In the study area, the OSD, which apparently formed in a deep-marine setting below the carbonate compensation depth (Turner et al. 2011), is divided into five members (Fig. 2). The bottom unit, the Transition Member, comprises a thin-bedded limestone and phyllite sequence that becomes more pelitic and carbonaceous up section, grading into dark gray, non-calcareous phyllite and phyllitic siltstone toward the top. This unit is overlain by the Siliceous Mudstone Member consisting of up to 50 m of pyritic, black siliceous mudstone in which pyrite is present as thin laminae, ovoid concretions, and disseminations. In sharp contact above occurs finely to thickly bedded gray to black, graptolite-bearing, recessive carbonaceous limestone and calcareous mudstone of the Calcareous Mudstone Member, which can reach a thickness of several hundred meters and has a sharp contact to the overlying unit. The Lower Cherty Mudstone Member is the primary V-bearing horizon at the Van Property, with reported grades of about 0.6% V_2O_5 over 50 m vertically and 700 m along strike. This unit is characterized by blocky fracturing, gray-black to black weathering, and uniform bedding of 3 to 15 cm occurring in cherty mudstone or siliceous argillite with an elevated siliceous content. Despite the relatively high silica content, the carbon content is higher than in the adjacent and, especially, underlying units. On weathered surfaces, secondary blue zinc and yellow vanadium minerals are reported. The unit is up to 100 m thick at the Van Property. It sharply changes into the last member of the OSD, the Upper Siliceous Mudstone Member, consisting of poorly laminated, well-cleaved, carbonaceous, and siliceous mudstone with abundant limestone concretions and can exceed 600 m thickness. The top of the unit is graptolite-bearing, constraining the age to Lower Devonian. An anomalous V-rich horizon of up to 21.5 m at 0.6% V_2O_5 occurs at the top of the unit. The contact with the overlying Earn Group is gradational.

The Lower Devonian to Middle Mississippian Earn Group, a turbiditic sequence, comprises the Portrait Lake and Prevost formations at the Van Property, of which the latter is the youngest unit preserved in the study area. The Portrait Lake Formation, 70 to 100 m thick, consists of carbonaceous chert and cherty argillite with limestone concretions and does not show cleavage. The Prevost Formation has non-siliceous to siliceous distal turbidites with a basal cross-laminated to parallel-laminated siltstone base that grades upward into a thicker, fine-grained argillite. Barite is common, and cleavage is well developed in the unit.

Although the study area did not undergo excessive deformation, relatively low-grade (sub-)greenschist metamorphism occurred during the Jurassic (e.g., Gordey and Roots 2011). The recent study by McGill et al. (2024) revealed metamorphic temperatures of 345–361 °C for the Van Property. Additionally, cleavage is common in all Paleozoic units at the Van Property. However, the Rabbitkettle Formation has two cleavages and small-scale open folds with east-trending axes, which are absent in the overlying Road River Group. This led to the assumption that the area underwent a period of deformation following the deposition of the Rabbitkettle Formation prior to the onset of Road River Group deposition (Carne and Gish 1999). Hence, more than one deformation event occurred.

Materials and Methods

A total of six samples were collected in the summer of 2005 at the Van Property by geologists of the Northwest Territories Geological Survey to characterize the composition and mineralogy of the prospect, with special attention paid to V-enriched horizons (Fig. 3; Table 1). Samples are from three stratigraphic levels listed from oldest to youngest: (1) Lower Cherty Mudstone Member, OSD (hf05-33 to -36; Figs. 3, 4a, and 4b); (2) Upper Siliceous Mudstone Member, OSD (hf05-37; Figs. 3 and 4c); and (3) Prevost Formation, Earn Group (hf05-38; Figs. 3 and 4d).

Various methods were applied to constrain the composition and mineralogy of the V-bearing siliceous argillite and siliceous mudstone at the Van Property. Details on whole-rock lithogeochemistry, X-ray diffraction (XRD), scanning electron microscopy (SEM), and electron microprobe analysis (EMPA) can be found in the Online Materials[1].

Results

Petrography

The siliceous argillite samples of the OSD are very fine-grained (<20 μm) with varying degrees of thickness and carbon content; the latter is especially prominent in samples with a sooty appearance. Some samples are cross-cut by millimeter- to centimeter-thick calciteveinlets (Fig. 4a). Yellow (e.g., secondary V minerals; Carne and Gish 1999) to brown weathering (i.e., gossan made of apparently secondary goethite) is common (Figs. 4b and 4c). The

Table 1. Summary of sample information and applied methods

Sample No.	Easting	Northing	Stratigraphy	Comment	TS	WR	SEM	EMPA
hf05-33	218177.4	6895523.9	OSDcm	Argillite with high-carbon content. Slicken-sided surface is highly glossy and fracture surface is coated with a crystalline film.	x	x	x	x
hf05-34	218177.4	6895523.9	OSDcm	Argillite with high-carbon content cut by calcite/barite veins.	x	x	–	–
hf05-35	218177.4	6895523.9	OSDcm	Argillite chip sample through the section.	–	x	–	–
hf05-36	217780.3	6895927.3	OSDcm	Argillite bearing a pale brown alteration along space cleavage. The rock contains minor veins of carbonate/barite parallel to cleavage. Pale white stylolites.	x	x	x	–
hf05-37	217773.8	6895019.4	OSDsm	Argillite with minor pale carbonate fractures. Pale white to gossanous coating on fracture surfaces.	x	x	x	x
hf05-38	218102.1	6894049.2	DPcm	Mudstone finely laminates with pale gray interbeds. The main cleavage is at an obtuse angle to the bedding. Similar appearance to the Active member.	x	x	x	–

Notes: Easting and Northing are based UTM NAD83 Zone 10. Abbreviations: DPcm = Prevost Formation, Earn Group; EMPA = electron microprobe analyses; OSDcm = Lower Cherty Mudstone Member, Duo Lake Formation; OSDsm = Upper Siliceous Mudstone Member, Duo Lake Formation; SEM = scanning electron microscopy; TS = thin section; WR = whole-rock lithogeochemistry; x = analyzed, "–" = not analyzed.

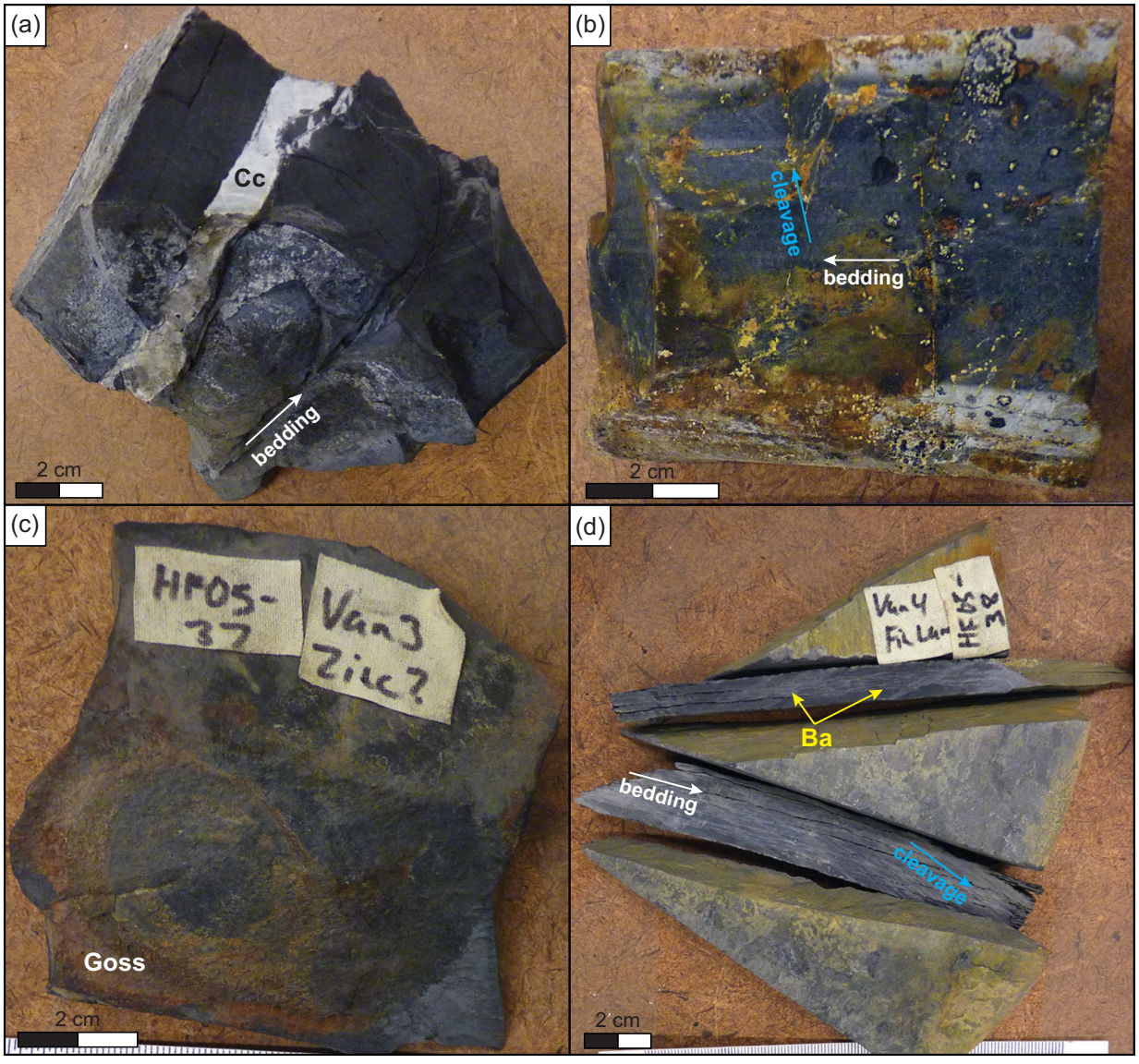

Figure 4. Samples from the Van Property. (**a** and **b**) Lower Cherty Mudstone Member, Duo Lake Formation; (**c**) Upper Siliceous Mudstone Member, Duo Lake Formation; and (**d**) Prevost Formation. (**a**) Thinly bedded siliceous argillite with high-carbon content cut by centimeter-thick calcite vein at angle to bedding (hf05-34); (**b**) thinly bedded, siliceous argillite with pale brown alteration, supposedly secondary V minerals, along space cleavage (hf05-36); (**c**) thinly bedded siliceous argillite and gossanous coating on fracture surfaces (hf05-37); (**d**) siliceous mudstone finely laminated with sub-millimeter, pale gray interbeds of barite. The main cleavage is at an obtuse angle to the bedding (hf05-38). Mineral abbreviations: Ba = barite; Cc = calcite; Goss = gossaneous. All scale bars are 2 cm.

sample from the Prevost Formation (hf05-38) is gray, fine-grained with millimeter-thick barite interbeds, yellow weathered surfaces, and prominent cleavage (Fig. 4d).

Mineralogy

The samples from the OSD were examined in more detail due to the V enrichment reported for these strata in Carne and Gish (1999) and Flavelle (2013), and the V concentration was determined by whole-rock analysis (see below). Their major mineral is quartz with minor to trace amounts of carbonaceous matter and traces of muscovite, illite, apatite, rutile, calcite, dolomite, and sulfides (i.e., pyrite, sphalerite; Fig. 5). Fine, aligned quartz schlieren with trace amounts of silicates alternate with black carbonaceous material (Fig. 5a), whereas carbonates, sulfides, and rutile are commonly disseminated in the quartz-rich matrix with no preferred orientation (Figs. 5b–5h).

Quartz (Figs. 5c and 5e) is the dominant phase and occurs as very fine-grained (<10 μm), sub-angular to sub-rounded grains of which the long axis is commonly aligned parallel to bedding. Convex-concave grain boundaries and triple junctions of ≈120° between adjacent grains (Fig. 5h) are indicative of pressure solution and recrystallization at (sub-)greenschist facies metamorphism (e.g., Becker 1995; Wenk et al. 2022). Carbonaceous matter (Figs. 5b–5h) is the second most abundant phase in the OSD samples. It is very fine-grained (<20 μm), flaky with amoeboid shapes, and is commonly found in occurrences between quartz grains and adjacent to illite, rutile, and sulfides. Although X-ray diffraction identified graphite, based on reflectance and the assumed *P-T* conditions [i.e., (sub-)greenschist facies], additional carbonaceous phases could not be unambiguously identified but are assumed to be present. Illite (Figs. 5c–5e) occurs as prismatic single grains within the quartz matrix and is commonly at an obtuse angle to the long axis of quartz grains; instead, it shows alignment parallel to cleavage than to bedding. Grains are up to 30 μm long, can show internal cleavage planes, can be kinked due to deformation, and rarely

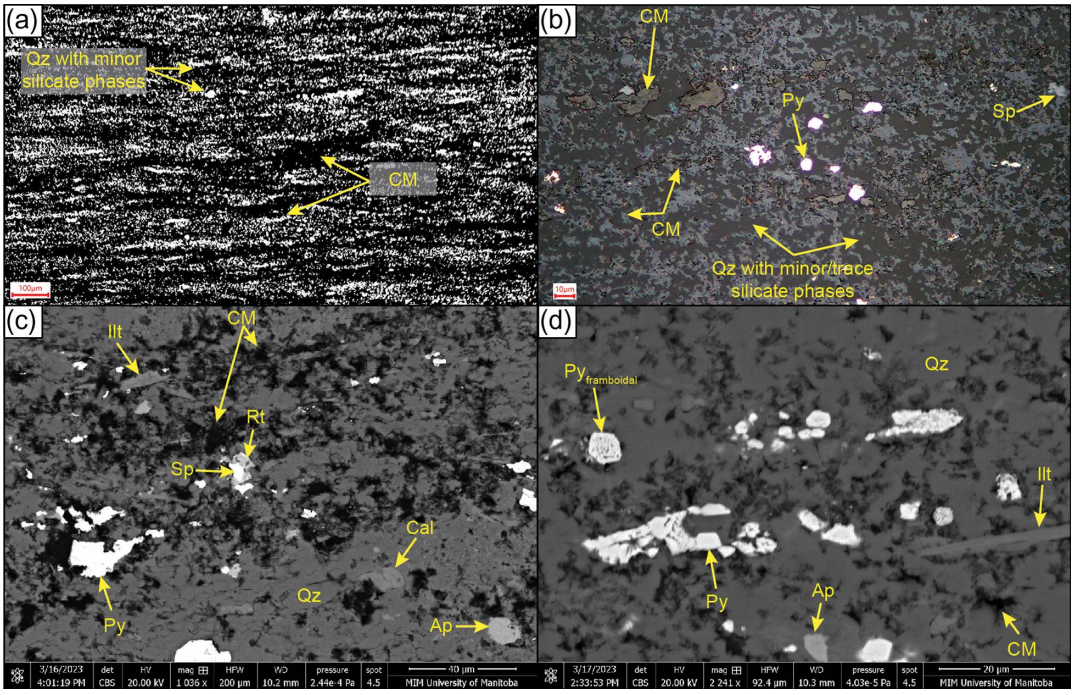

Figure 5. Transmitted and reflected light and backscattered electron (BSE) images of siliceous argillite, Duo Lake Formation. (**a**) Finely laminate siliceous argillite with alternating beds of very finely grained quartz and trace silicate phases with carbonaceous matter (transmitted light, parallel Nichols). (**b**) Finely disseminated pyrite in matrix of quartz with trace silicate phases and carbonaceous matter (reflected light). (**c**) Quartz-rich matrix with interstitial carbonaceous matter–illite–disseminated pyrite, sphalerite, rutile–apatite–calcite. Prismatic illite aligned parallel lamination and surrounded by graphite. Sphalerite is rimmed by rutile and surrounded by graphite-quartz. Quartz is sub-angular to sub-roundish with the long axis aligned parallel to bedding and recrystallized with convex-concave grain boundaries caused by pressure solution (BSE). (**d**) Quartz-rich matrix with interstitial carbonaceous matter–illite–rutile–prismatic and framboidal pyrite. Framboidal pyrite occurring as single disseminated grains or with prismatic pyrite in matrix. Both illite and pyrite are partly in contact with carbonaceous matter (BSE). (**e**) Pyrite with rutile and dolomite in quartz-rich matrix with interstitial carbonaceous matter–illite. Illite is aligned parallel to bedding, partly weakly kinked (upper left) and with pyrite inclusion (right). Quartz is sub-angular to sub-roundish with the long axis aligned parallel to bedding and recrystallized with convex-concave grain boundaries caused by pressure solution (BSE). (**f**) Pyrite with marginal rutile in quartz-rich matrix with interstitial carbonaceous matter–illite–apatite. Both carbonaceous matter and illite are partly in contact with pyrite and rutile. Rutile has inclusions of pyrite (BSE). (**g**) Sphalerite with rutile in quartz-rich matrix with calcite and interstitial graphite. Rutile has sphalerite inclusions (BSE). (**h**) Sphalerite with marginal rutile and in contact with carbonaceous matter in quartz-rich matrix (BSE). Quartz is sub-roundish and recrystallized with convex-concave grain boundaries and triple junctions of ≈120° between three adjacent grains (BSE). Mineral abbreviations after Whitney and Evans (2010): Ap = apatite; Cal = calcite; CM = carbonaceous matter; Dol = dolomite; Ilt = illite; Py = pyrite; $Py_{framboidal}$ = framboidal pyrite; Qz = quartz; Rt = rutile; Sp = sphalerite. *(Figure Continous on Next page.)*

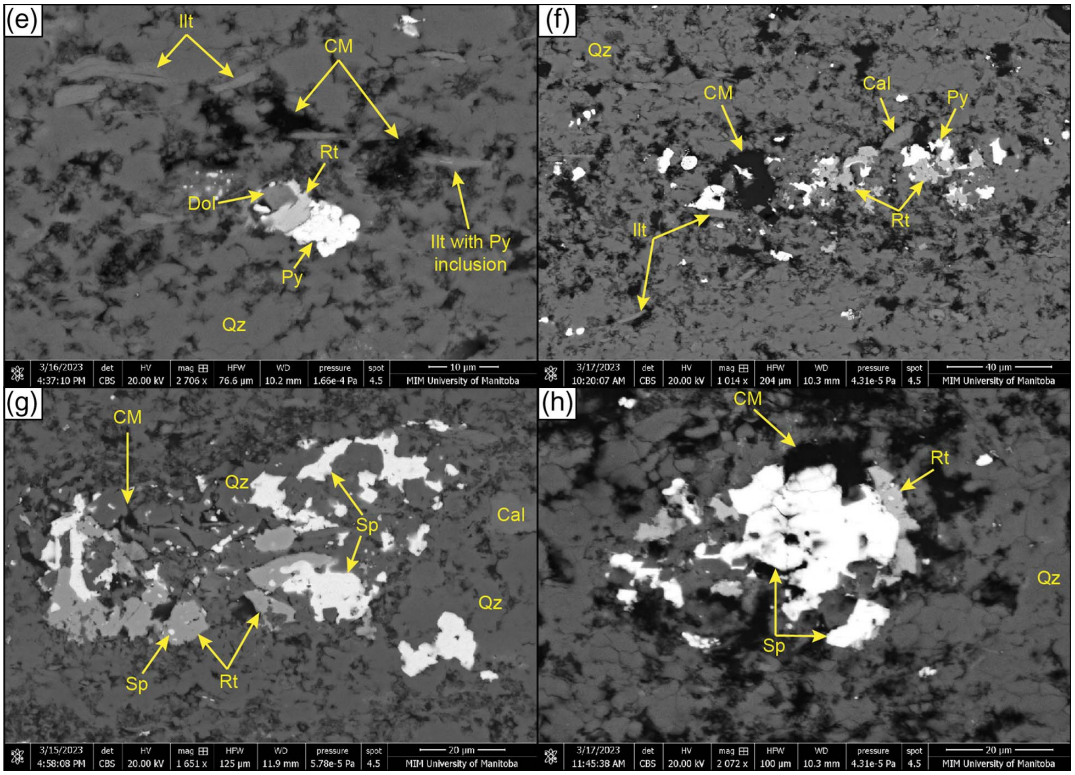

FIGURE 5.—*CONTINUED.*

TABLE 2. Geochemical summary of major and minor elements for the Van Property (Prevost Formation and Duo Lake Formation), other metalliferous shales and cherts from literature and non-metalliferous black shale SDO-1

Location	Mecca Quarry Shale					Van Property							
Stratigraphy	Linton Fm				Prevost Fm	Duo Lake Fm							
Lithology (Herron 1988)	(non-)calcareous black shale				non-calcareous siliceous shale	(non-)calcareous argillaceous chert							
Relative metal content[a]	metalliferous				non-metalliferous	metalliferous							
Age	Pennsylvanian				Lower Devonian to Middle Mississippian	Lower Ordovician to Devonian							
Source	Coveney and Martin (1983)					This study				Carne and Gish (1999)			
n	Av 5	Std 5	Min 5	Max 5	Av 1	Av 5	Std 5	Min 5	Max 5	Av 19	Std 19	Min 19	Max 19
SiO_2 (wt%)	35.2	12.6	25.3	57.0	82.4	80.6	9.17	68.1	94.0				
Al_2O_3	11.1	3.67	7.31	17.1	10.6	2.32	0.52	1.52	2.85	1.60	0.66	0.51	3.06
Fe_2O_3t	4.66	0.83	3.50	5.42	0.37	1.03	0.25	0.65	1.33	1.12	0.38	0.79	2.47
CaO	1.64	1.20	0.59	3.58	0.12	2.82	4.27	0.09	10.3	5.16	5.30	0.16	18.35
MgO	1.37	0.23	1.12	1.65	0.33	0.43	0.17	0.24	0.69	1.46	2.13	0.17	6.75
Na_2O	0.61	0.07	0.54	0.69	0.11	0.03	0.01	0.01	0.04				
K_2O	2.29	0.83	1.59	3.74	2.44	0.68	0.14	0.47	0.84	0.40	0.13	0.17	0.61
Cr_2O_3					0.01	0.01	0.00	0.01	0.02				
TiO_2	0.49	0.17	0.31	0.77	0.46	0.12	0.03	0.08	0.15	0.03	0.03	0.01	0.08
MnO						0.01	0.00	0.01	0.02	0.01	0.01	0.00	0.02
P_2O_5	1.38	1.35	0.20	3.40	0.02	0.49	0.66	0.04	1.66	0.52	0.59	0.08	2.09
BaO					1.21	0.05	0.02	0.03	0.07				
LOI	39.4	14.2	14.0	56.9	3.70	11.5	3.85	4.82	14.2				
Total					102	100	1.05	99.3	102				
C					1.08	8.24	2.81	3.52	11.0	8.05	1.75	4.53	10.20
S					0.04	0.82	0.49	0.16	1.42	0.58	0.37	0.20	1.26
TOC	28.8	13.9	3.80	46.5	0.99	7.85	3.21	3.33	10.9	6.89	1.59	3.80	9.35
C_{inorg}										1.28	1.51	0.05	5.00
$C_{graphite}$					0.11	3.96	2.06	0.96	5.40				
V_2O_5	0.80	0.53	0.16	1.80	0.12	0.53	0.17	0.25	0.69	0.48	0.18	0.19	0.72
$\log(SiO_2/Al_2O_3)$	0.50	0.04	0.43	0.54	0.89	1.55	0.15	1.40	1.79				
$\log(Fe_2O_3t/K_2O)$	0.32	0.16	0.04	0.42	–0.82	0.18	0.08	0.05	0.23				

(Table extends onto next page.)

have minute sulfide inclusions. Illite is in contact with carbonaceous matter on at least one surface and can occur spatially close to sulfides and rutile. Rutile (Figs. 5c and 5e–5h) is amoeboid, <10 μm in size, and occurs most commonly in direct contact with either pyrite or sphalerite, forming rutile-sulfide aggregates; rutile can have minute, round sulfide inclusions. Rutile-sulfide aggregates have no preferred orientation, are randomly disseminated, and occur adjacent to carbonaceous matter. Disseminated rutile occurs rarely as isolated grains within the quartz-rich matrix. Pyrite and sphalerite are of similar abundance and occur as disseminated grains within the quartz-rich matrix with no preferred orientation. Pyrite (Figs. 5c–5f) is commonly amoeboid in shape, less commonly prismatic, and rarely framboidal. Sphalerite (Figs. 5c, 5g, and 5h) has amoeboid shapes, is intergrown with rutile, and forms in direct contact with carbonaceous matter. Other trace phases such as muscovite, calcite, dolomite, and apatite (Figs. 5c and 5e–5g) occur as very small (<15 μm), disseminated, subhedral to anhedral, single grains in the quartz-rich matrix. Calcite and dolomite are also observed in close contact with rutile-sulfide aggregates.

Deformation is most prominently developed in recrystallized quartz grains and kinked illite (Figs. 5e and 5h). Pyrite and sphalerite can show cataclastic cracks formed under brittle conditions.

Whole-rock lithogeochemistry

Results from major, minor, and trace element composition of siliceous argillite (OSD) and siliceous mudstone (Prevost Formation) at the Van Property are summarized in Tables 2 and 3, and the complete data set is found in the Online Materials[1].

The compositions of the analyzed samples differ between those from the OSD (hf05-33 to -37) and the younger Prevost Formation (hf05-38). Although samples from the OSD are from different stratigraphic members (i.e., hf05-37: Upper Siliceous Mudstone Member; hf05-33 to -36: Lower Cherty Mudstone Member), their major to trace element compositions are similar (Online Materials[1]).

Using the chemical classification of Herron (1988) to distinguish between shales and sands by utilizing log ratios of SiO_2/Al_2O_3 and Fe_2O_3t/K_2O, samples from the OSD cannot be defined as (black) shales (Fig. 6a). Instead, they are referred to as siliceous argillite here due to their relatively high SiO_2 content and $\log(SiO_2/Al_2O_3)$ ratio (Fig. 6a). This is also in accordance with the nomenclature used in the previous study at the Van Property by Carne and Gish (1999). Additionally, these siliceous argillites vary in CaO concentration (Herron 1988), with most samples being non-calcareous (CaO < 2.8 wt%) and only one sample classifying as calcareous (CaO = 2.8–10.7 wt%, Fig. 6b). The sample from the Prevost Formation classifies as non-calcareous siliceous mudstone (Fig. 6). In the OSD siliceous argillites, the Al_2O_3 (2.32 ± 0.52 wt%), K_2O (0.68 ± 0.14 wt%), Na_2O (0.03 ± 0.01 wt%), TiO_2 (0.12 ± 0.03 wt%), and BaO (0.05 ± 0.02 wt%) contents are lower relative to the younger siliceous mudstone (Figs. 7a–7b;

Table 2. (*Continued*)

Location	Moss				Storsjøn-Myrvikken				Zhongcun				SDO-1
Stratigraphy	Road River Group				Alum Shale Formation				Shuigouku Formation				
Lithology (after Herron 1988)	(non-)calcareous black shale and siliceous shale				siliceous shale				(non-)calcareous siliceous shale and argillaceous chert				non-calcareous black shale
Relative metal content[a]	metalliferous				metalliferous				metalliferous				non-metalliferous
Age	Late Cambrian to Middle Devonian				Cambrian				Cambrian				Devonian
Source	Gadd et al. (2019)				Leventhal (1991)				Fu et al. (2023)				Huyck (1991), GeoReM (2023)
	Av	Std	Min	Max	Av	Std	Min	Max	Av	Std	Min	Max	Av
n	9	9	9	9	5	5	5	5	13	13	13	13	1
SiO_2 (wt%)	59.3	11.2	42.3	73.9	50.8	1.84	48.8	52.8	75.8	13.7	55.5	94.8	49.3
Al_2O_3	14.0	2.00	11.7	17.5	6.58	0.42	6.30	7.30	3.87	2.83	0.40	7.54	12.3
Fe_2O_3t	2.22	1.59	1.00	4.40	4.26	0.83	3.40	5.60	2.25	1.72	0.28	5.00	9.34
CaO	2.07	2.93	0.05	7.84					1.37	1.86	0.03	5.97	1.05
MgO	1.97	1.60	0.83	5.12					0.53	0.48	0.08	1.87	1.54
Na_2O	0.30	0.28	0.06	0.70					0.02	0.01	0.01	0.04	0.38
K_2O	3.27	0.45	2.49	3.93	3.48	0.26	3.20	3.80	1.70	1.52	0.13	4.06	3.35
Cr_2O_3									0.10	0.12	0.01	0.39	
TiO_2	0.73	0.14	0.48	0.94					0.14	0.10	0.01	0.26	0.71
MnO	0.02	0.02	0.00	0.06	0.06	0.01	0.05	0.07	0.01	0.00	0.01	0.01	0.04
P_2O_5	0.14	0.10	0.02	0.28					0.50	0.89	0.01	2.99	0.11
BaO									0.57	0.60	0.06	2.27	
LOI	8.86	2.26	7.26	10.5					11.1	6.39	1.40	21.2	21.7
Total	99.1	0.5	98.7	99.4					99.5	0.45	99.1	100.90	
C	3.02	1.27	2.12	3.92									9.95
S	2.14	1.69	0.68	5.86	4.70	1.01	3.60	6.30	0.11	0.33	0.00	1.21	5.35
TOC	2.71	0.63	1.70	3.90	12.9	0.85	11.8	13.8	7.47	4.78	0.17	15.80	9.68
C_{inorg}													
$C_{graphite}$													
V_2O_5	0.23	0.05	0.16	0.32	0.36	0.11	0.27	0.55	1.28	1.44	0.23	4.52	0.03
$\log(SiO_2/Al_2O_3)$	1.09	0.50	0.65	2.31					0.56	0.19	0.29	0.88	1.13
$\log(Fe_2O_3t/K_2O)$	18.3	2.32	14.7	22.0					5.72	4.41	0.55	11.60	16.71

Notes: Av = average; C_{inorg} = inorganic carbon; LOI = loss on ignition; Max = maximum value; Min = minimum value; n = number of samples; Std = standard deviation; TOC = total organic carbon.

[a] Relative metal content follows the definition after Huyck (1991) in which a metalliferous shale is a "shale that is enriched in any given metal by a factor of 2× (except beryllium, cobalt, molybdenum, and uranium, for which 1× is sufficient) relative to the U.S. Geological Survey Standard SDO-1." Non-metalliferous implies that there is no significant metal enrichment relative to SDO-1.

Table 3. Geochemical summary of trace elements, including rare earth elements for the Van Property (Prevost Formation and Duo Lake Formation), other metalliferous shales and cherts from literature and non-metalliferous black shale SDO-1

Location	Mecca Quarry Shale				Van Property								
Stratigraphy	Linton Formation				Prevost Formation	Duo Lake Formation							
Lithology (Herron 1988)	(non-)calcareous black shale				calcareous siliceous shale	(non-)calcareous argillaceous chert							
Relative metal content[a]	metalliferous				non-metalliferous	metalliferous							
Age	Pennsylvanian				Lower Devonian to Middle Mississippian	Lower Ordovician to Devonian							
Source	Coveney and Martin (1983)				This study					Carne and Gish (1999)			
n	Av 5	Std 5	Min 5	Max 5	Av 1	Av 5	Std 5	Min 5	Max 5	Av 19	Std 19	Min 19	Max 19
Ba (ppm)						504	126	313	644	211	85.8	90.0	370
Cr					70.0	96.5	28.9	50.0	130	114	41.3	22.0	178
Cs					4.53	1.40	0.34	1.04	1.90	0.56	0.17	0.50	1.00
Ga					15.8	4.52	0.82	3.20	5.20				
Ge													
Hf					2.30	0.86	0.21	0.60	1.10				
Nb					7.40	2.26	0.53	1.70	3.00				
Rb					119	24.1	4.74	16.8	28.9				
Sn					1.00								
Sr					35.4	42.9	49.0	9.20	127	73.21	76.44	5.00	304
Ta					0.50	0.16	0.05	0.10	0.20				
Th					5.56	1.76	0.48	1.16	2.40				
U	120	63.0	70.0	230	3.29	8.15	2.81	4.00	11.90	10.00	0.00	10.00	10.00
V	4500	2950	900	10 100	675	2943	978	1380	3870	2704	1036	1045	4040
W					1.00	0.95	0.10	0.80	1.00				
Zr					82.0	42.3	10.5	26.0	55.0				
As					2.00	45.2	22.0	9.70	67.1	68.0	34.2	22.0	146
Bi					0.14	0.04	0.01	0.03	0.05				
Hg					0.06	0.92	0.36	0.35	1.28	0.78	0.44	0.12	1.00
In						0.01	0.00	0.01	0.01				
Re					0.02	0.12	0.06	0.03	0.15				
Sb					1.64	21.5	11.4	4.64	33.7	27.1	49.4	2.00	216.00
Se	242	97.6	110	400	1.10	49.0	26.6	6.60	76.0				
Te					0.02	0.09	0.03	0.04	0.11				
Tl					0.19	0.67	0.46	0.12	1.40				
Ag						2.05	0.93	1.30	3.40	1.26	0.85	0.20	3.20
Cd						60.8	61.4	4.50	130	41.2	28.9	1.50	114.50
Co					0.50	0.72	0.49	0.50	1.60	5.53	17.34	0.50	77.00
Cu	236	170	75.0	500	2.00	103	108	16.0	282	84.9	56.6	0.51	240.00
Li					20.0	10.0	0.00	10.0	10.0	2.68	0.95	1.00	4.00
Mo	707	486	200	1550	2.00	41.7	19.7	17.0	67.3	53.9	23.4	18.0	97.0
Ni	404	258	35.0	800	3.00	160	108	32.0	285	112.74	58.77	26.0	243.00
Pb	178	139	100	500	11.0	173	370	3.00	835	6.78	4.01	2.00	16.0
Sc					9.00	3.40	0.89	2.00	4.00				
Zn	4481	4454	500	14300	19.0	3665	3637	335	7870	2169	1492	146	5860
La					21.8	10.4	4.83	5.70	18.0	8.90	3.30	0.09	10.0
Ce					41.0	10.3	4.95	7.00	18.9				
Pr					5.02	2.90	1.17	1.38	4.51				
Nd					18.4	12.9	5.32	5.40	19.5				
Sm					3.04	2.94	1.32	0.97	4.30				
Eu					0.48	0.71	0.36	0.21	1.10				
Gd					1.90	3.25	1.47	0.99	4.66				
Tb					0.29	0.53	0.26	0.16	0.83				
Dy					1.94	3.31	1.64	0.95	4.89				
Ho					0.40	0.75	0.35	0.21	1.05				
Er					1.30	2.22	1.05	0.66	3.21				
Tm					0.18	0.34	0.15	0.11	0.46				
Yb					1.24	2.22	1.00	0.69	3.13				
Lu					0.21	0.38	0.17	0.13	0.55				
Ce/Ce*[b]					0.93	0.49	0.10	0.37	0.61				
Ce/Ce*[c]					0.90	0.44	0.10	0.33	0.57				
Eu/Eu*[d]					0.93	1.05	0.10	0.92	1.16				
REE+Y					110	83.7	37.2	33.2	130				
Y/Ho					32.3	40.5	1.80	37.8	42.7				
La_N/Sm_N					1.28	0.68	0.22	0.50	1.05				
Sm_N/Yb_N					1.23	0.67	0.07	0.58	0.76				

Notes: Abbreviations: Av = average; Max = maximum value; Min = minimum value; n = number of samples; Std = standard deviation.[a] Relative metal content follows the definition after Huyck (1991) in which a metalliferous shale is a "shale that is enriched in any given metal by a factor of 2× (except beryllium, cobalt, molybdenum, and uranium, for which 1× is sufficient) relative to the U.S. Geological Survey Standard SDO-1." Non-metalliferous implies that there is no significant metal enrichment relative to SDO-1.[b] Ce anomaly after Lawrence et al. (2006): $Ce/Ce^* = Ce_N/(Pr^2/Nd)_N$.[c] Ce anomaly after Nozaki (2008): $Ce/Ce^* = 2Ce_N/(La_N + Pr_N)$.[d] Eu anomaly after McLennan (1989): $Eu/Eu^* = Eu_N/(Sm \times Gd)_N^{1/2}$; N is normalization to PAAS (McLennan 1989).

(Table extends onto next page.)

TABLE 3.—*EXTENDED*

Location	Moss				Storsjøn-Myrvikken				Zhongcun				SDO-1
Stratigraphy	Road River Group				Alum Shale Formation				Shuigouku Formation				
Lithology (Herron 1988)	(non-)calcareous black shale and siliceous shale				siliceous shale				(non-)calcareous siliceous shale and argillaceous chert				non-calcareous black shale
Relative metal content[a]	metalliferous				metalliferous				metalliferous				non-metalliferous
Age	Late Cambrian to Middle Devonian				Cambrian				Cambrian				Devonian
Source	Gadd et al. (2019)				Leventhal (1991)				Fu et al. (2023)				Huyck (1991), GeoReM (2023)
n	Av 9	Std 9	Min 9	Max 9	Av 5	Std 5	Min 5	Max 5	Av	Std	Mi	Max	Av
Ba (ppm)	25 831	54 459	1745	170 000	1620	694	1000	2600	4153	3023	533	9580	397
Cr	87.8	37.0	36.0	140	111	55.3	85.0	210	742	874	90.0	2950	66.4
Cs	9.50	2.26	7.90	11.1									6.90
Ga	17.7	4.03	14.8	20.5									16.8
Ge	0.20	0.00	0.20	0.20									1.30
Hf	3.46	0.75	2.40	4.40									4.70
Nb	8.70	0.71	8.20	9.20									11.4
Rb	143	23.7	113	178									126
Sn	3.00	0.00	3.00	3.00									3.70
Sr	280	221	47.0	630									75.1
Ta	1.19	0.55	0.69	2.10									1.10
Th	8.67	1.49	6.56	10.00					56.1	40.7	1.88	127	10.5
U	9.39	3.73	4.02	15.0	201	39.82	134	240	3.29	2.22	0.41	6.37	48.8
V	1274	285	890	1787	2020	630	1500	3100	7178	8088	1270	25 300	160
W	1.30	0.71	0.80	1.80									3.30
Zr	100	0.00	100	100									
As	46.6	39.6	19.2	126									68.5
Bi	0.25	0.04	0.22	0.27									
Hg	290	70.7	240	340									0.19
In	0.07	0.03	0.03	0.11									
Re	0.11	0.09	0.04	0.17									0.09
Sb	19.6	4.00	13.6	24.0									
Se	48.1	39.8	12.0	123									
Te	0.23	0.09	0.10	0.40									
Tl	7.81	6.83	1.40	20.0									
Ag	1.07	1.09	0.10	2.80									0.16
Cd	6.82	9.76	0.20	23.0									0.31
Co	5.98	3.63	1.00	11.0	22.8	0.84	22.0	24.0	9.06	6.64	0.40	22.2	46.8
Cu	24.5	26.7	1.00	66.0	132	13.0	120	150					60.2
Li													28.6
Mo	46.9	31.1	16.0	110	312	44.4	250	350					134
Ni	134	110	34	390	470	40.5	415	510	257	233	13.7	816	99.5
Pb	14.3	3.89	6.00	19.9	55.0	23.2	35.0	85.0					27.9
Sc	12.4	1.67	10.0	15.0									13.2
Zn	318	421	12	990	440	110	320	565					64.1
La	40.7	18.1	20.0	83.0					24.1	14.0	3.30	47.1	38.5
Ce	65.7	25.1	39.0	123					25.6	16.1	3.50	52.5	79.3
Pr	9.12	4.37	5.30	19.0					5.61	3.27	0.75	11.2	8.90
Nd	32.4	14.7	19.0	65.0					24.4	14.9	3.20	53.7	36.6
Sm	4.65	2.03	2.39	8.30					5.41	3.42	0.59	12.6	7.70
Eu	0.82	0.44	0.34	1.50					1.30	0.87	0.13	2.98	1.60
Gd	3.33	1.69	1.41	6.20					7.69	5.38	0.64	17.6	7.40
Tb	0.50	0.20	0.25	0.86					1.19	0.82	0.10	2.45	1.20
Dy	3.08	1.10	1.63	5.00					8.16	5.76	0.66	17.9	6.00
Ho	0.64	0.21	0.36	1.00					2.02	1.50	0.17	4.66	1.20
Er	1.84	0.53	1.23	2.70					6.32	4.96	0.48	15.7	3.60
Tm	0.32	0.08	0.20	0.43					0.90	0.71	0.08	2.29	0.45
Yb	2.15	0.42	1.46	2.70					5.47	4.34	0.43	14.2	3.40
Lu	0.35	0.07	0.23	0.43					0.84	0.66	0.07	2.14	0.54
Y	22.1	8.18	12.3	35.0					83.8	64.5	5.80	205	40.6
Ce/Ce*[b]	0.82	0.08	0.69	0.93					0.63	0.17	0.31	0.90	1.13
Ce/Ce*[c]	0.80	0.05	0.71	0.87					0.53	0.15	0.23	0.78	0.98
Eu/Eu*[s]	0.94	0.13	0.75	1.10					0.94	0.05	0.82	1.00	0.99
REE+Y	188	63.4	120	326					203	123	19.9	378	237
Y/Ho	34.1	2.56	29.4	37.1					40.7	5.16	32.7	51.0	33.8
La_n/Sm_n	1.65	0.47	0.91	2.29					0.82	0.21	0.51	1.10	0.89
Sm_n/Yb_n	1.09	0.50	0.65	2.31					0.56	0.19	0.29	0.88	1.13

Table 2). In contrast, SiO_2 (80.6 ± 9.17 wt%), Fe_2O_3t (1.03 ± 0.25 wt%), total organic carbon (TOC; 7.9 ± 3.2 wt%), and S (0.82 ± 0.49 wt%) contents are higher relative to the siliceous mudstone from the younger Prevost Formation (Figs. 7c–7d; Table 2).

The trace element concentrations between the different stratigraphic horizons at the Van Property also vary (Figs. 7e–7h and 8; Table 3). Samples from the OSD show enrichments in some metals exceeding twice the concentration of SDO-1, the reference black shale of the U.S. Geological Survey (Huyck 1991;

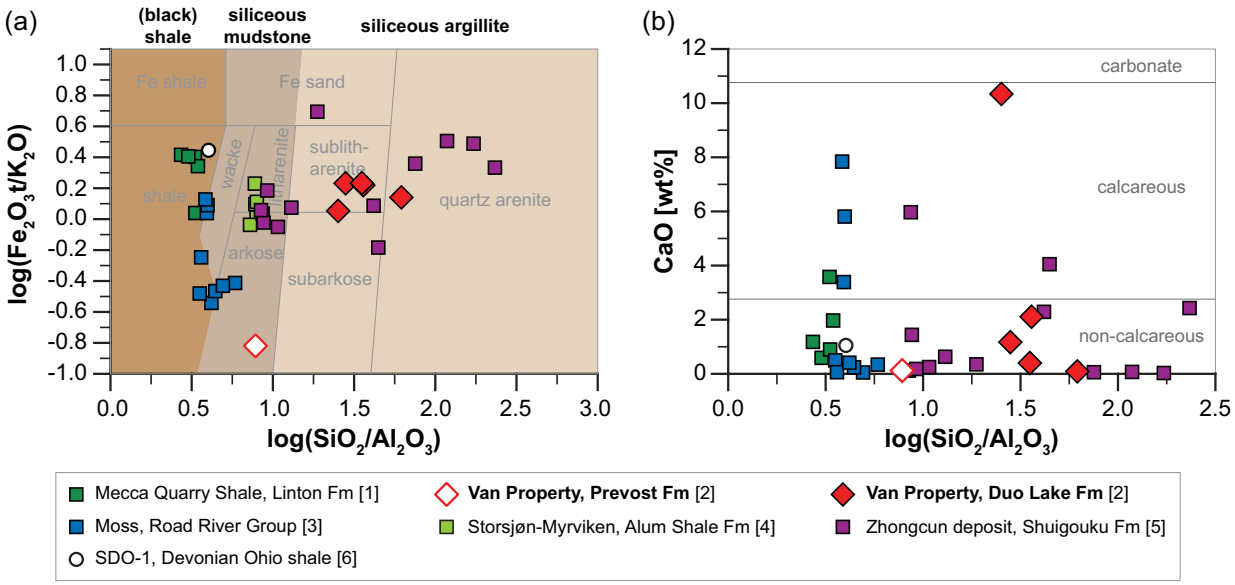

Figure 6. Geochemical classification of sand and shale after Herron (1988). (**a**) $\log(SiO_2/Al_2O_3)$ vs. $\log(Fe_2O_3t/K_2O)$ distinguishing clay-rich rocks (shale) from silica-rich rocks (wacke, arenite, arkose, quartz sand). (**b**) $\log(SiO_2/Al_2O_3)$ vs. CaO [wt%] defining Ca content of sedimentary rocks. Non-calcareous: CaO < 2.8 wt% (Ca < 4 wt%); calcareous: CaO = 2.8–10.7 wt% (Ca = 4–15 wt%); and carbonate: CaO > 10.7 wt% (Ca > 15 wt%). Note: Highlighted fields distinguishing between (black) shale (dark brown), siliceous mudstone (medium brown), and siliceous argillite (light brown) are based on $\log(SiO_2/Al_2O_3)$ projected to $\log(Fe_2O_3t/K_2O) = 0$ with (black) shale = $\log(SiO_2/Al_2O_3) < 0.71$, siliceous shale = $0.71 < \log(SiO_2/Al_2O_3) < 1.05$, and siliceous argillite = $\log(SiO_2/Al_2O_3) > 1.05$. Data source: [1] Mecca Quarry shale: Coveney and Martin (1983); [2] Van Property: this study; [3] Moss: Gadd et al. (2019); [4] Storsjøn-Myrvikken: Leventhal (1991); [5] Zhongcun deposit: Fu et al. (2023); [6] SDO-1: Huyck (1991) and Jochum et al. (2005). SDO-1 is non-metalliferous black shale. Abbreviation: Fm = Formation.

Jochum et al. 2005), defining the investigated samples as metalliferous following Huyck (1991). In contrast, the siliceous mudstone of the Prevost Formation is non-metalliferous. In particular, V and Zn are strongly enriched in the OSD with average concentrations of 2943 ± 978 ppm and 3665 ± 3637 ppm, respectively, compared to 675 ppm V and 19 ppm Zn in the Prevost Formation. Furthermore, the siliceous argillites of the OSD have higher contents of U (8.15 ± 2.81 ppm vs. 3.29 ppm, Fig. 7f), Ni (160 ± 108 ppm vs. 3 ppm, Fig. 7g), Mo (41.7 ± 19.7 ppm vs. 2 ppm, Fig. 7h), Cu (103 ± 108 ppm vs. 2 ppm, Fig. 8), and As (45.2 ± 22 ppm vs. 2 ppm). In contrast, concentrations of Cr, W, and Co are similar between lithologies of both stratigraphic levels (Table 3). The (non-)calcareous siliceous argillites from the OSD show weak-to-strong positive correlations of V with various elements, including Al_2O_3 ($R^2 = 0.74$, Fig. 8a), K_2O ($R^2 = 0.62$, Fig. 8b), TiO_2 ($R^2 = 0.53$, Fig. 8c), S ($R^2 = 0.89$, Fig. 8d), TOC ($R^2 = 0.85$, Fig. 8e), U ($R^2 = 0.58$, Fig. 8f), Ni ($R^2 = 0.92$, Fig. 8g), Mo ($R^2 = 0.54$, Fig. 8h), Zn ($R^2 = 0.45$, Fig. 8i), and Cu ($R^2 = 0.28$, Fig. 8j).

Rare earth elements + Y (REE+Y) have relatively low total concentrations in both the OSD and Prevost Formation with sums of 83.7 ± 32.7 ppm and 110 ppm, respectively (Table 3). In samples from the OSD, the REE+Y pattern normalized to Post-Archean Australian Shale (PAAS; McLennan 1989) shows a strong Ce anomaly [Ce/Ce* = 0.49 ± 0.1 and 0.44 ± 0.1 after Lawrence et al. (2006) and Nozaki (2008), respectively] and no Eu anomaly [Eu/Eu* = 1.05 ± 0.1 after McLennan (1989); Fig. 9; Table 3]. The REE pattern increases slightly from light to heavy REE and Y. The REE pattern of the Prevost Formation sample is characterized by neither a significant Ce [Ce/Ce* = 0.93 and 0.9 after Lawrence et al. (2006) and Nozaki (2008), respectively] nor Eu anomaly [Eu/Eu* = 0.93 after McLennan (1989)], with a relatively flat pattern that shows a weak decrease from light to heavy REEs and Y (Fig. 9).

X-ray diffraction (XRD)

Results from XRD are provided in Table 4. Although samples from both the OSD and Prevost Formation are dominated by quartz (OSD: 82.1%, Prevost: 73.4%), their mineralogy varies (Fig. 10), consistent with their differing geochemistry. In the OSD samples, the second most common phase is carbonaceous matter (identified as graphite), followed by muscovite. However, based on reflectance studies using reflected light microscopy at the University of Manitoba, kerogen or bitumen likely are present as well. Hydrocarbon speciation done by SGS Canada Inc. did not reveal the composition of carbonaceous matter. The results from both methods were inconclusive. Additional mineral phases that occur commonly in the siliceous argillite, albeit at trace (<2%) levels, are illite, pyrite, sphalerite, calcite, dolomite, fluor-apatite, and rutile (Fig. 5). Most illite is of the $2M_1$ polytype based on XRD spectra with the presence of characteristic peaks at d = 4.48 Å (021) and 2.42 Å (117). The *c* parameter of unit cells of the best-fitting illite also is ~20 Å, confirming the presence of the 2*M* polytype [personal communication A. Zhang (2023)]. Biotite, gypsum, and goethite are not observed microscopically but by XRD, totaling <2% on average. The most prominent differences between siliceous argillite (OSD) and siliceous mudstone (Prevost Formation) are the enrichment in muscovite and the occurrence of barite,

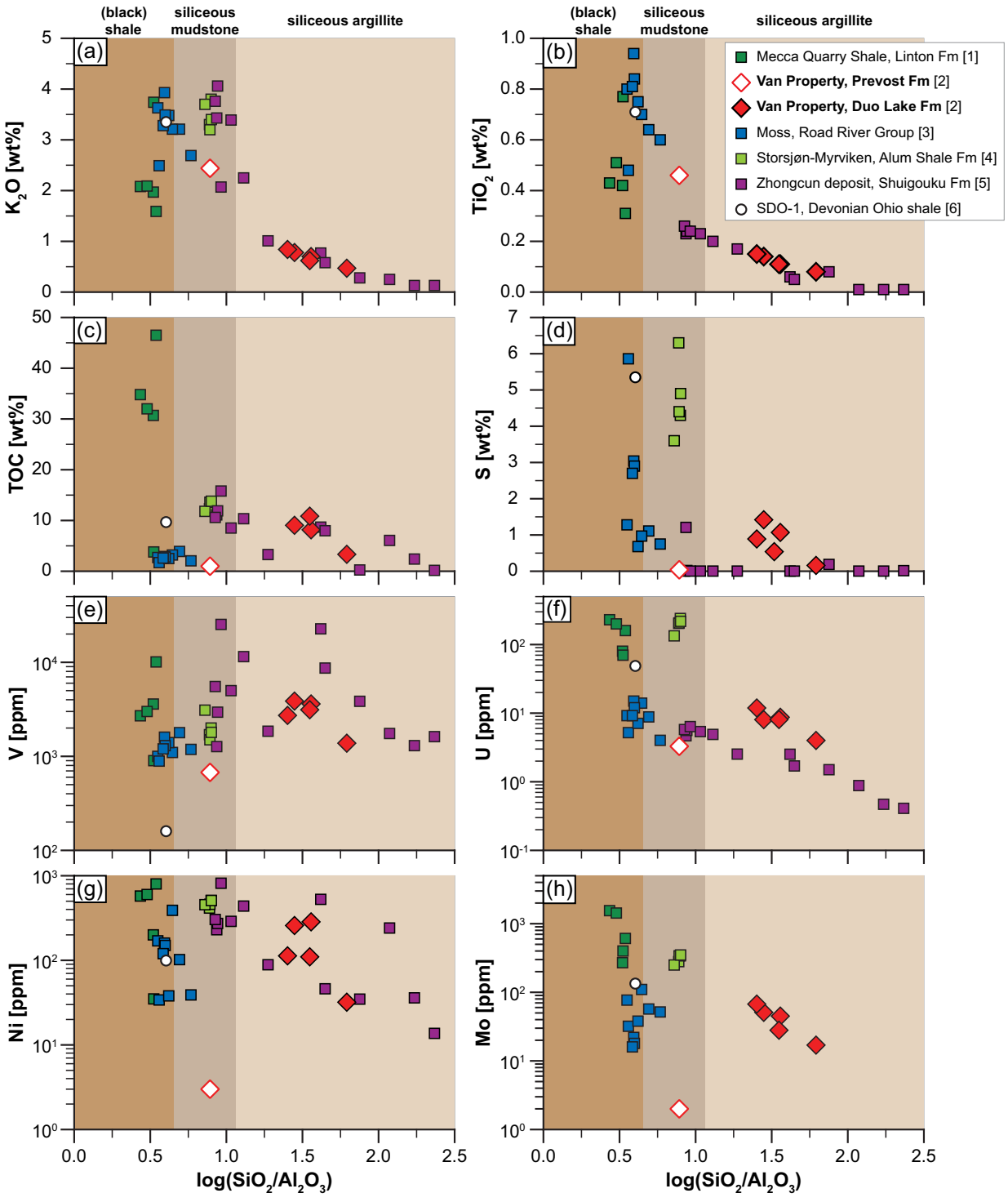

Figure 7. Selected major, minor, and trace elements vs. $\log(SiO_2/Al_2O_3)$. (**a**) TiO_2 [wt%]. (**b**) K_2O [wt%]. (**c**) Total organic carbon (TOC) [wt%]. (**d**) S [wt%]. (**e**) V [ppm]. (**f**) U [ppm]. (**g**) Ni [ppm]. (**h**) Mo [ppm]. Note: Highlighted fields distinguishing between (black) shale (dark brown), siliceous mudstone (medium brown), and siliceous argillite (light brown) are based on $\log(SiO_2/Al_2O_3)$ projected to $\log(Fe_2O_3t/K_2O) = 0$ with (black) shale = $\log(SiO_2/Al_2O_3) < 0.71$, siliceous shale = $0.71 < \log(SiO_2/Al_2O_3) < 1.05$, and siliceous argillite = $\log(SiO_2/Al_2O_3) > 1.05$. Data source: [1] Mecca Quarry shale: Coveney and Martin (1983); [2] Van Property: this study; [3] Moss: Gadd et al. (2019); [4] Storsjøn-Myrvikken: Leventhal (1991); [5] Zhongcun deposit: Fu et al. (2023); [6] SDO-1: Huyck (1991) and Jochum et al. (2005). SDO-1 is non-metalliferous black shale. Abbreviation: Fm = Formation.

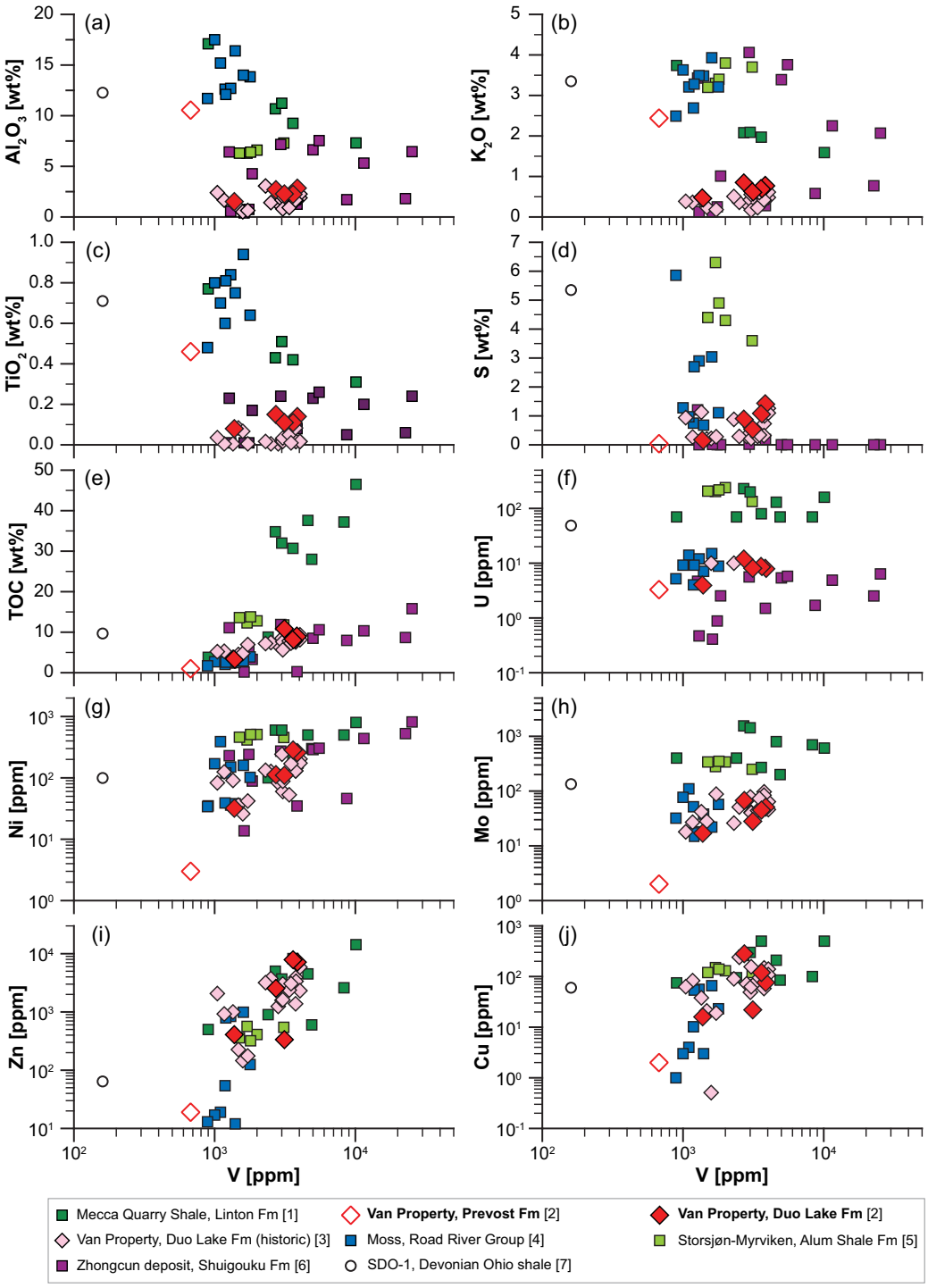

Figure 8. Selected major, minor, and trace elements vs. V [ppm]. (**a**) Al_2O_3 [wt%]. (**b**) K_2O [wt%]. (**c**) TiO_2 [wt%]. (**d**) S [wt%]. (**e**) Total organic carbon (TOC) [wt%]. (**f**) U [ppm]. (**g**) Ni [ppm]. (**h**) Mo [ppm]. (**i**) Zn [ppm]. (**j**) Cu [ppm]. Data source: [1] Mecca Quarry shale: Coveney and Martin (1983); [2] Van Property: this study; [3] Van Property: Carne and Gish (1999); [4] Moss: Gadd et al. (2019); [5] Storsjøn-Myrvikken: Leventhal (1991); [6] Zhongcun deposit: Fu et al. (2023); [7] SDO-1: Huyck (1991) and Jochum et al. (2005). SDO-1 is non-metalliferous black shale. Abbreviation: Fm = Formation.

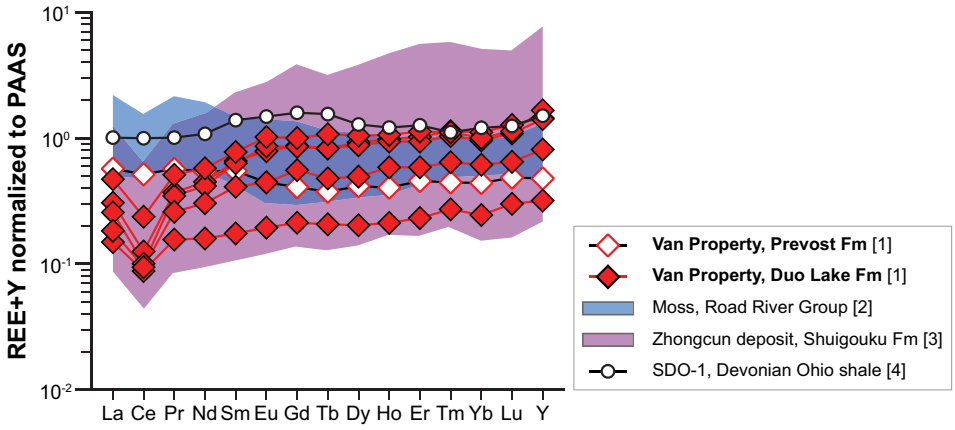

Figure 9. REE and Y normalized to Post-Archean Australian Shale (PAAS) after McLennan (1989). Data source: [1] Van Property: this study; [2] Moss: Gadd et al. (2019); [3] Zhongcun deposit: Fu et al. (2023); [4] SDO-1: Huyck (1991) and Jochum et al. (2005). SDO-1 is non-metalliferous black shale. Abbreviation: Fm = Formation.

Table 4. Summary of semiquantitative XRD results for analyzed samples from the Van Property

Mineral	Hf05-33	Hf05-34	Hf05-36	Hf05-37	Hf05-38	Hf05-39
Quartz (wt%)	77.0	78.4	90.8	81.5	73.4	2.5
Calcite	0.8	2.5	–	–	–	90.2
Muscovite	5.6	4.6	2.6	3.9	20.7	–
Graphite	9.3	8.0	3.6	10.3	1.0	–
Pyrite	1.4	1.0	0.2	0.9	–	0.1
Dolomite	0.8	0.5	–	–	0.4	1.5
Albite	–	–	–	–	–	3.2
Gypsum	1.0	1.0	0.3	0.4	–	0.3
Biotite	0.6	0.2	0.4	0.8	–	–
Sphalerite	1.2	1.1	0.1	–	–	–
Fluorapatite	0.3	0.4	–	0.3	–	0.3
Gibbsite	–	–	–	–	1.6	0.2
Phlogopite	–	–	–	–	0.1	1.2
Goethite	–	0.1	0.1	–	–	0.3
Rutile	0.4	0.4	0.4	0.4	0.5	–
Barite	–	–	–	–	0.3	–
Illite	1.7	1.7	1.5	1.6	2.1	0.1
Total	100	100	100	100	100	100

gibbsite, and phlogopite in the latter. Moreover, sulfides are absent, and graphite is a trace phase in the Prevost Formation.

Mineral phases with V as a major component reported from other shale-hosted V deposits [e.g., roscoelite and mannardite (Fu et al. 2023; Yang et al. 2023)] and Jim and Janice Creeks near the study location, NWT (Carne and Gish 1999), were not identified by XRD or SEM; V is only present in minor or trace concentrations in some identified phases. Secondary V-bearing phases (e.g., corvusite) or V-bearing sulfides (e.g., sulvanite), as reported by Carne and Gish (1999), were not identified via XRD or SEM in the studied samples. Common minerals hosting minor V in shale deposits are illite, oxides, and potentially carbonaceous matter (Fester et al. 1927; Fischer et al. 1968; Peacor et al. 2000; Di Cecco et al. 2018; Lu et al. 2021; Veselovský et al. 2021). To further constrain the V host(s) in siliceous argillite at the Van Property, SEM and EMPA were applied to the V-rich samples of the OSD.

Scanning electron microscopy (SEM) and electron microprobe analysis (EMPA)

Mapping by SEM and EMPA. All phases of interest (i.e., illite, rutile, carbonaceous matter) are very fine-grained (<30 µm), and detailed elemental maps done both via energy-dispersive spectrometry (EDS) on SEM and wavelength-dispersive spectrometry (WDS) on EMPA were utilized to determine the spatial distribution of V (Fig. 11). The most prominent V counts are observed both in rutile and some illite (Fig. 11) that have been in close contact with carbonaceous matter; sulfides occur with V-bearing rutile as well but do not show any V counts (Figs. 11a and 11h). In general, V signals recorded by EDS are strongest in rutile (Figs. 11b and 11i); the presence of V in this oxide was

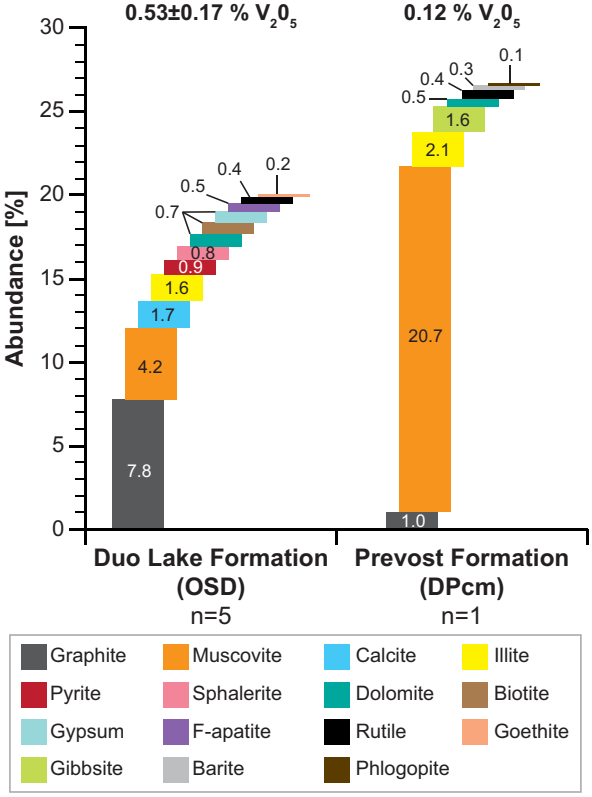

Figure 10. Results from XRD analyses on samples from OSD and Prevost Formation. Non-quartz fraction is shown for siliceous argillite of older OSD and siliceous mudstone of Prevost Formation.

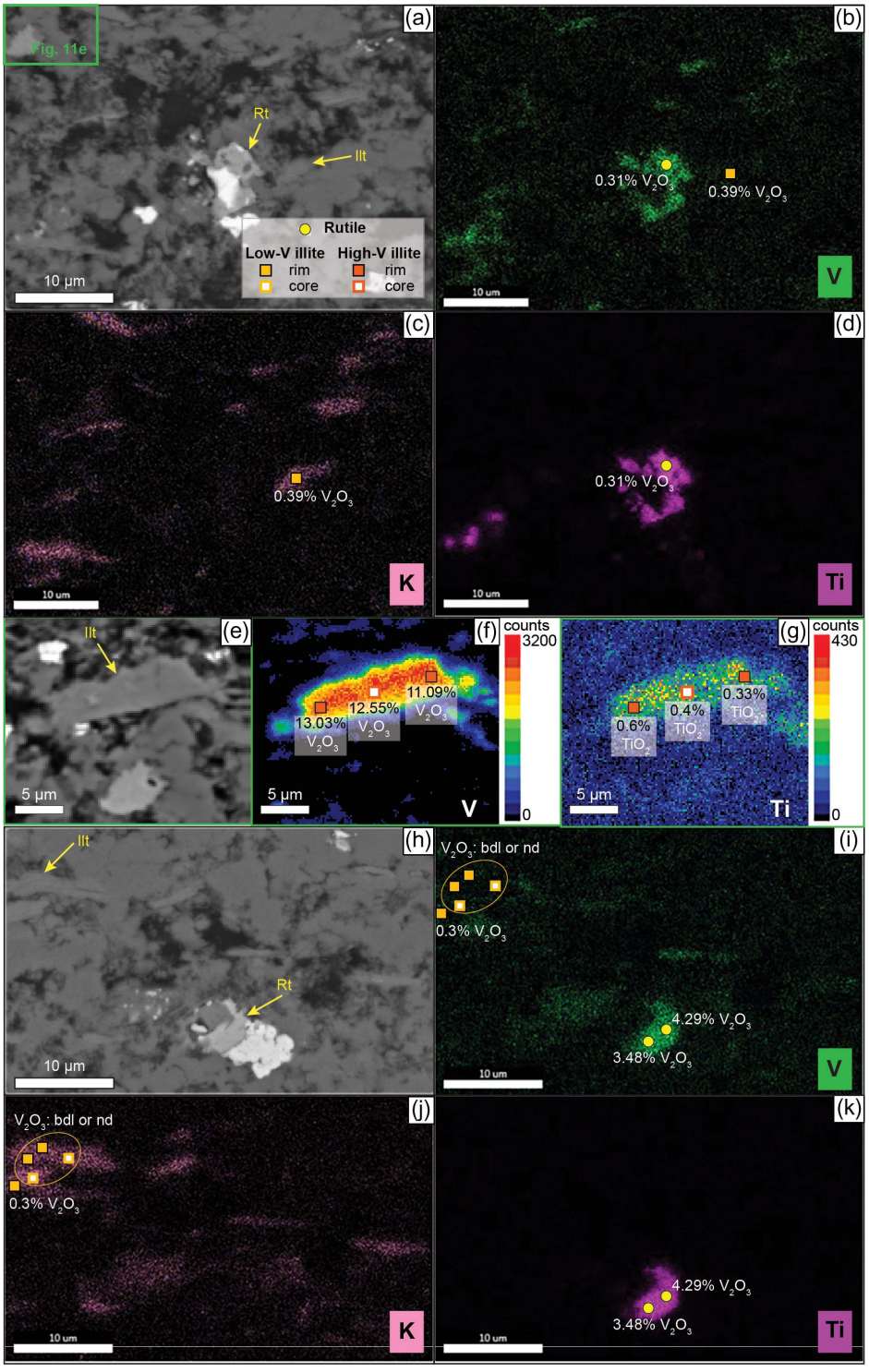

Figure 11. BSE images of selected rutile and illite grains with EDS and WDS elemental maps of siliceous argillite (OSD). (**a**–**d**). Rutile with sphalerite and adjacent low-V illite in quartz-rich matrix with carbonaceous matter. (**a**) BSE image, which is a close-up of Figure 5c. The green rectangle in the upper left refers to part **e**. (**b**) EDS elemental map of **a** showing the occurrence of V. Data represent V concentration of illite and rutile done by EMPA. (**c**) EDS elemental map of **a** showing K and highlighting the occurrence of illite. Vanadium content in illite analyzed by EMPA is also shown. (**d**) EDS elemental map of **a** showing Ti and highlighting the occurrence of rutile. Vanadium content in rutile analyzed by EMPA is also shown. (**e**–**g**) High-V illite with sphalerite in the quartz-rich matrix and in contact with carbonaceous matter. (**e**) BSE image, which is a close-up of Figure 5c and part **a** (green rectangle). (**f**) WDS elemental map of illite showing V counts. Zoning with high counts in core and lower counts at rim is due to overlap of 1 µm beam spots on a small area. Individual data represent V content analyzed by EMPA. (**g**) WDS elemental map of illite showing Ti counts. Individual data represent Ti content analyzed by EMPA. (**h**–**k**) Rutile between pyrite and dolomite in the quartz-rich matrix. Illite is partly kinked and in contact with carbonaceous matter. (**h**) BSE image, which is a close-up of Figure 5e. (**i**) EDS elemental map of **h** showing the occurrence of V. Data represent V concentration of illite and rutile done by EMPA. Circle refers to analyses with V content below detection limit or none detected. (**j**) EDS elemental map of **h** showing K and highlighting the occurrence of illite. Vanadium content in illite analyzed by EMPA is also shown. The circle refers to analyses with V content below detection limit or none detected. (**k**) EDS elemental map of **h** showing Ti and highlighting the occurrence of rutile. Vanadium content in rutile analyzed by EMPA is also shown. Abbreviations: bdl = below detection limit; Ilt = illite; nd = not detected; Rt = rutile.

confirmed by observing spectra on the *K*β peak that do not interfere with Ti emission lines. Vanadium signals were recorded in carbonaceous matter (Figs. 11b and 11i) by EDS; however, the signal is weak and may represent background. It was not possible to confirm the occurrence of V in this phase, most likely due to relatively low abundance and hardness contrast to neighboring phases impacting the polishing of carbonaceous matter and hence its analyses by X-rays. Since neither mapping method allowed for quantitative assessment of V in illite and rutile, EMPA was utilized on selected grains in siliceous argillite.

EMPA. Electron microprobe analyses were utilized to quantify the V content in both illite and rutile identified as V-bearing

Table 5. Summary of EMPA results on low-V illite, high-V illite, and rutile and their calculated mineral formula based on 11 O atoms and two O atoms for illite and rutile, respectively

Mineral	Low-V illite (n = 23)				High-V illite (n = 9)				Rutile (n = 6)			
	Av	Std	Min	Max	Av	Std	Min	Max	Av	Std	Min	Max
Al_2O_3 (wt%)	30.2	3.28	23.1	35	23.7	1.27	21.8	25.8	0.11	0.01	0.10	0.11
MgO	1.75	0.92	0.47	5.29	2.36	0.69	1.79	4.11	0.09		0.09	0.09
Na_2O	0.46	0.24	0.16	1.05	0.12	0.01	0.12	0.13				
CaO									0.35	0.07	0.28	0.47
SiO_2	49.2	2.39	45.5	57.4	49.7	3.56	45.7	55.4	1.00	0.25	0.68	1.31
K_2O	9.60	0.80	7.21	10.6	5.88	0.31	5.42	6.30				
TiO_2	0.30	0.13	0.13	0.66	0.32	0.14	0.18	0.60	93.8	2.22	90.2	95.4
FeO	2.44	1.57	0.62	6.47	0.75	0.03	0.73	0.77				
V_2O_3	0.78	0.59	0.3	1.91	10.3	2.32	7.13	13.1	1.66	1.75	0.31	4.29
H_2O	5.55	1.66	2.94	10.8	7.35	1.60	5.44	10.7				
Total	99.9	0.08	99.7	100	99.8	0.18	99.6	100	97.1	0.35	96.6	97.5
Total_no water	94.4	1.66	89.1	97.1	92.5	1.56	89.3	94.2				
	Mineral calculations, O = 11								Mineral calculations, O = 2			
Al (apfu)	2.39	0.23	1.83	2.75	1.90	0.12	1.69	2.08	0.00	0.00	0.00	0.00
Mg	0.18	0.09	0.05	0.53	0.24	0.07	0.18	0.41	0.01		0.01	0.01
Na	0.05	0.03	0.00	0.14	0.01	0.01	0.00	0.02				
Ca									0.02	0.00	0.01	0.02
Si	3.30	0.13	3.11	3.71	3.38	0.18	3.15	3.64	0.04	0.01	0.03	0.05
K	0.82	0.08	0.59	0.95	0.51	0.03	0.45	0.56				
Ti	0.02	0.01	0.01	0.03	0.02	0.01	0.01	0.03	2.91	0.03	2.86	2.95
Fe	0.14	0.09	0.03	0.40	0.01	0.02	0.00	0.05				
V	0.02	0.03	0.00	0.10	0.56	0.13	0.38	0.73	0.03	0.03	0.01	0.07
Total	6.92	0.10	6.58	7.07	6.63	0.08	6.48	6.72	3.00	0.00	3.00	3.00
OH	2.00	0.00	2.00	2.00	2.00	0.00	2.00	2.00				
Total+OH	8.92	0.10	8.58	9.07	8.63	0.08	8.48	8.72				
Si^{iv}	3.30	0.13	3.11	3.71	3.38	0.18	3.15	3.64				
Al^{iv}	0.70	0.13	0.29	0.89	0.62	0.18	0.36	0.85				
Sum_Tetrahedral	4.00	0.00	4.00	4.00	4.00	0.00	4.00	4.00				
Al^{vi}	1.69	0.14	1.37	1.86	1.29	0.08	1.16	1.40				
Fe^{vi}	0.14	0.09	0.03	0.40	0.01	0.02	0.00	0.05				
Mg^{vi}	0.18	0.09	0.05	0.53	0.24	0.07	0.18	0.41				
Ti^{vi}	0.02	0.01	0.01	0.03	0.02	0.01	0.01	0.03				
Sum_Octahedral	2.02	0.04	1.89	2.08	1.55	0.10	1.42	1.70				
V	0.02	0.03	0.00	0.10	0.56	0.13	0.38	0.73				
Sum_Octahedral+V	2.04	0.04	1.91	2.12	2.11	0.05	2.02	2.17				
Na	0.05	0.03	0.00	0.14	0.01	0.01	0.00	0.02				
K	0.82	0.08	0.59	0.95	0.51	0.03	0.45	0.56				
Sum_Interlayer	0.88	0.07	0.66	0.95	0.52	0.04	0.45	0.57				
4Si[a]	0.83	0.03	0.78	0.93	0.85	0.04	0.79	0.91				
M^{+a}	0.88	0.07	0.66	0.95	0.52	0.04	0.45	0.57				
$3R^{2a}$	0.10	0.05	0.05	0.23	0.08	0.02	0.06	0.14				

Notes: Av = average; Max = maximum value; Min = minimum value; n = number of samples; Std = standard deviation.
[a] Clay composition was calculated using Newman and Brown (1987) and is displayed in Figure 12.
4Si = Si/4, $M^+ = K + Na + 2Ca$, $3R^2 = (Fe^{2+} + Mg^{2+} + Mn^{2+})/3$, all elements in apfu

by both EDS and WDS mapping. The results for both phases are provided in Table 5 and the Online Materials[1].

Based on V-content, two illite compositions are identified: (1) low-V illite with <2 wt% V_2O_3 (Figs. 11a–11c and 11h–11j) and (2) high-V illite with >7 wt% V_2O_3 (Figs. 11e and 11f) of which the former is more common. Both variations are, however, similar in texture (Fig. 11), with the most prominent difference being that low-V illite commonly has cleavage developed and can be kinked (Figs. 11a–11c and 11h–11j). Both low-V and high-V illite are in contact with carbonaceous matter (Fig. 11). The composition of illite based on interlayer occupancy [i.e., illite-smectite with K = 0.5–0.69 atoms per formula unit (apfu) after Aja 1989 and Rosenberg 2002; illite end-member with K = 0.88 apfu after Meunier and Velde (1989); Środoń et al. (1992); Yates and Rosenberg (1997); Aja (2020)] was further constrained using the ternary plot after Newman and Brown (1987) and Aja (2020) (Fig. 12). This plot employs the silica content in the tetrahedral position (4Si), the sum of interlayer cations (M^+), and the sum of mafic elements on the octahedral site ($3R^2$) to distinguish between different clay end-members (Fig. 12a). Low-V illite is close to end-member composition of illite (K = 0.88 apfu; Fig. 12b) with a calculated average (n = 23) formula $K_{0.82}(Al_{1.69}Fe_{0.14}Mg_{0.18}Ti^{4+}_{0.02}V^{3+}_{0.02})^{vi}_{2.04}(Si_{3.30}Al_{0.70})^{iv}_{4.00}O_{10}(OH)_2\ (H_2O)$ (Table 5; Online Materials[1]). In contrast, high-V illite is much closer to the illite-smectite composition (K = 0.50–0.69 apfu) and has strong deficits on the interlayer site (Fig. 12b) with an average (n = 7) formula of $K_{0.51}(Al_{1.29}Fe_{0.01}Mg_{0.24}Ti^{4+}_{0.02}V^{3+}_{0.56})^{vi}_{2.11}(Si_{3.38}Al_{0.62})^{iv}_{4.00}O_{10}(OH)_2\ (H_2O)$ (Table 5; Online Materials[1]). Besides V content, low-V and high-V illite also have significantly different concentrations of Al_2O_3, FeO, K_2O, and Na_2O; low-V illite is enriched in all these elements relative to high-V illite (Fig. 13; Table 5). Vanadium also shows different element associations in each type of illite. In low-V illite, V is <0.17 apfu and is negatively correlated with Al^{3+} in the octahedral site; other correlations of V with elements in different sites are not observed (Figs. 13a–13e). In contrast, in high-V illite, the V correlates with several elements (Figs. 13a–13c and 13e), including Si and Al in the tetrahedral site, Al on the octahedral site, and Ti. When the size of the illite grains permitted, analyses close to the rim and core were

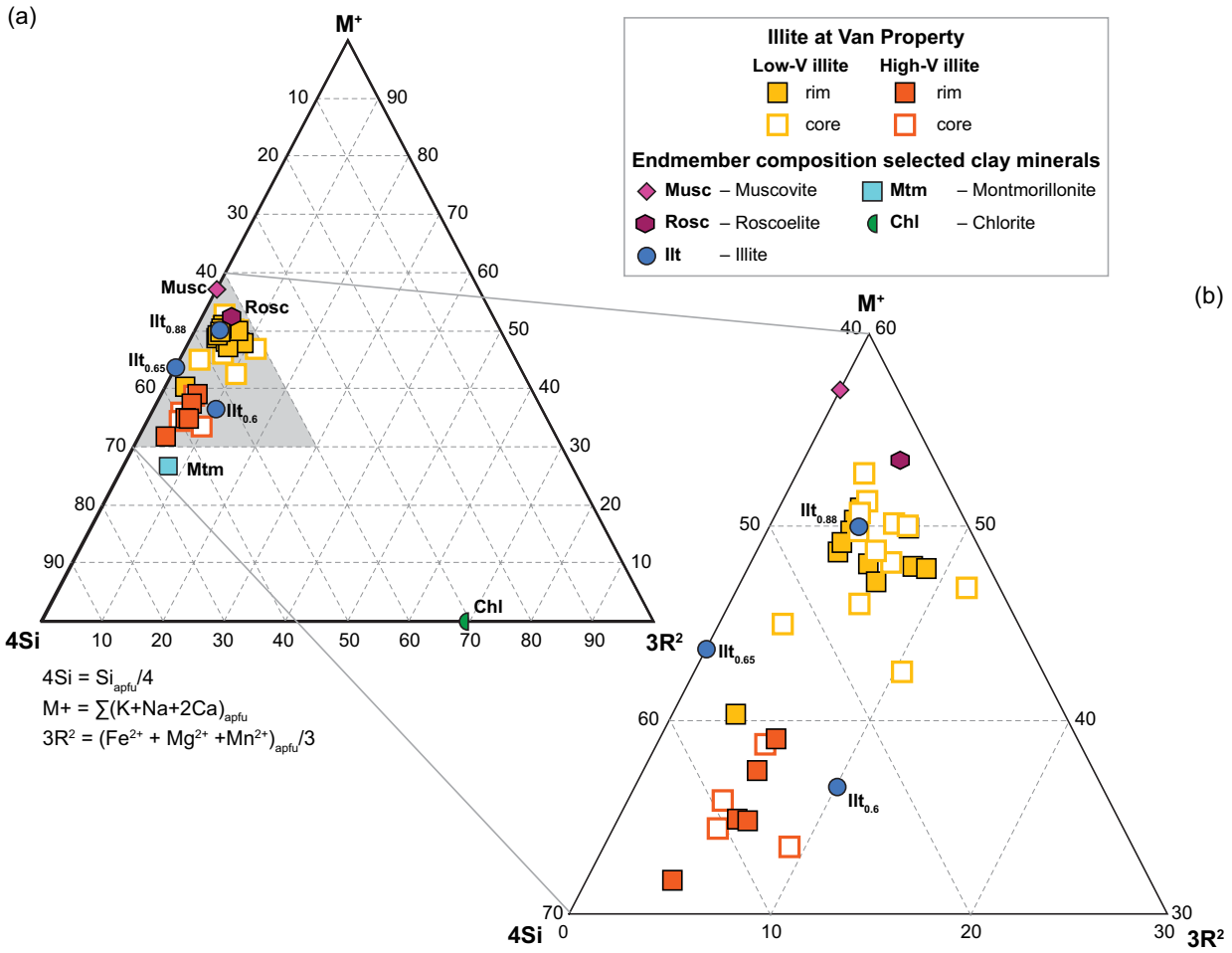

Figure 12. Composition of analyzed illite displayed in the 4Si-M^{+}-$3R^{2}$ ternary plot after Newman and Brown (1987) and Aja (2020). End-member composition of selected clay minerals are given for comparison (Rieder et al. 1998; Brigatti et al. 2003; IMA 2021) (**a**) Analyzed low-V illite (yellow) plots close to illite composition with interlayer charges of 0.88 ($Ilt_{0.88}$), whereas high-V illite (orange) plots near illite with interlayer charges of 0.6 ($Ilt_{0.60}$), 0.65 ($Ilt_{0.65}$), and smectite montmorillonite (Mtm). (**b**) Close-up of **a** showing the distribution of low-V illite close to end-member illite composition ($Ilt_{0.88}$) and high-V illite close to illite-smectite (I/S) composition. None of the analyzed illite grains is of roscoelite composition. The partial overlap between low-V illite from the Van Property and roscoelite is due to similar interlayer charges. Vanadium content is not considered in the plot.

performed, but no significant differences in composition were observed (Figs. 11 and 13; Online Materials[1]).

The small size of rutile grains made it difficult to avoid analyzing neighboring phases. Of the nine spots that were initially analyzed, only six analyses with totals of >97.3 wt% were used. Although these totals are relatively low for oxides and rutile, analyses showed trace concentrations of SiO_2 (1.00 ± 0.25 wt%) and CaO (0.35 ± 0.07 wt%), most likely due to overlaps with adjacent quartz and/or calcite, the composition of the analyzed rutile grains was stoichiometrically homogeneous with an average (n = 6) formula of $(Ti_{2.93}V_{0.03})_{2.91}$. Deficiencies in Ti^{4+} were attributed to the minute grain size and contamination with SiO_2 and CaO from neighboring grains. After TiO_2 (93.8 ± 2.22 wt%), V_2O_3 (1.66 ± 1.75 wt%) was the second most abundant element in rutile. Similar to illite, V concentrations in rutile were variable, with some spots having less than 0.80 wt% V_2O_3 (Figs. 11b and 11d) and other spots with 3.48 wt% V_2O_3 (Figs. 11i and 11k).

Discussion

Comparison to other shale-hosted V deposits

Shale-hosted V deposits are one of four major sub-classes of V deposits [i.e., vanadiferous titanomagnetite deposits, sandstone-hosted deposits, shale-hosted deposits, and vanadate deposits, e.g., Fischer and Stewart (1961); Fischer (1968, 1975); Fischer et al. (1968); Kelley et al. (2017)]. None of the approximately 20 globally known shale-hosted V deposits (Kelley et al. 2017; Elbokl 2022; Fu et al. 2023; Yang et al. 2023) are currently in production. Reasons include current limits on the effective beneficiation of V due to the fine-grained nature of host lithology and potential occurrence of V with organic matter (Vitolo et al. 2000; Li et al. 2021; Simandl and Paradis 2022) as well as a poorly developed deposit model. The deposit model does not account for variations in host lithology, V-bearing mineralogy, type and maturity of carbonaceous matter (i.e., kerogen, bitumen, or graphite), metamorphic grade, or what these characteristics imply for V enrichment process(es).

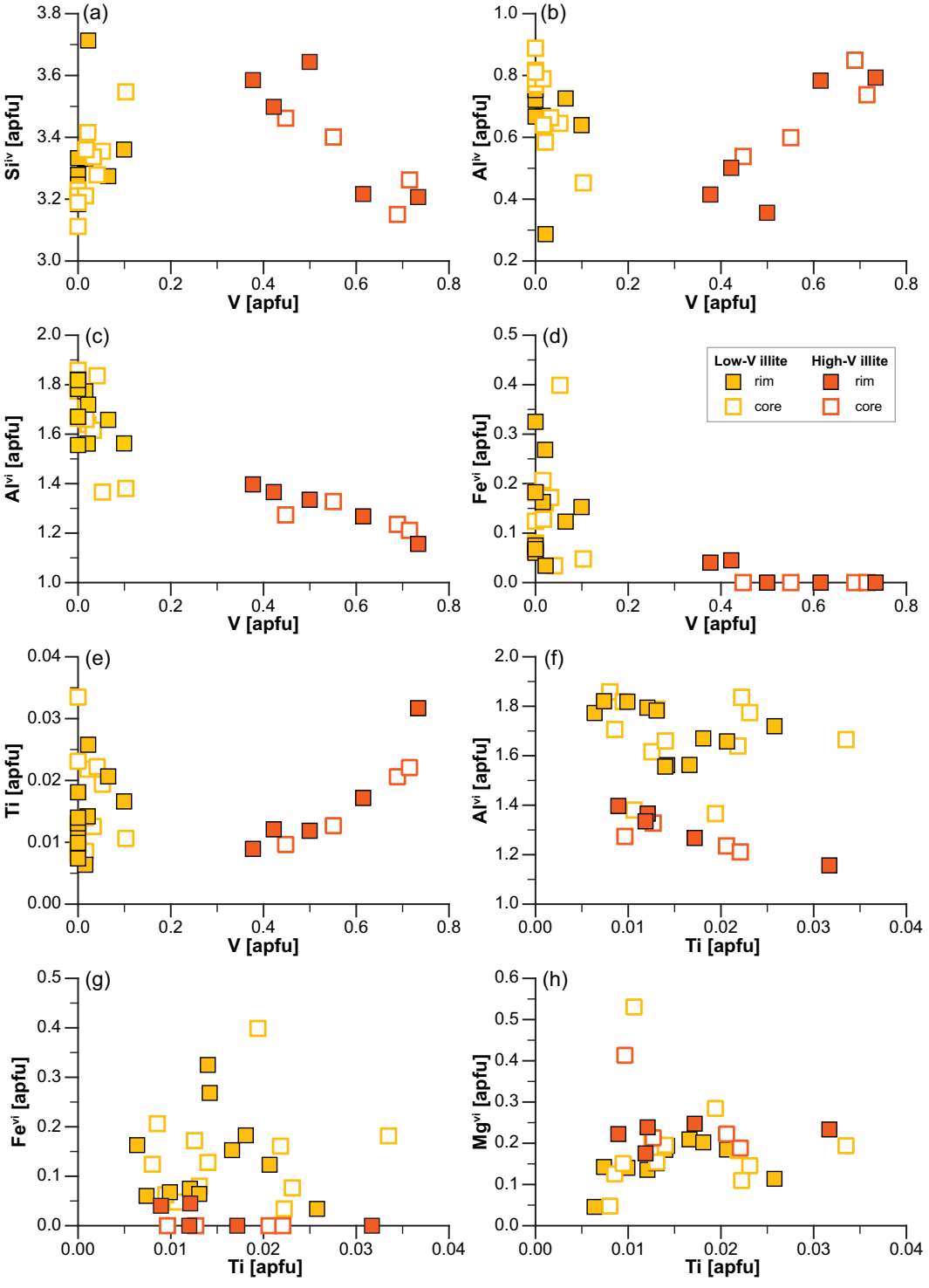

Figure 13. Binary plots displaying the composition of analyzed low-V and high-V illite (core and rim) in siliceous argillite of the OSD. All elements are in atoms per formula unit [apfu]. (**a**) V vs. Si^{iv}. (**b**) V vs. Al^{iv}. (**c**) V vs. Al^{vi}. (**d**) V vs. Fe^{vi}. (**e**) V vs. Ti. (**f**) Ti vs. Al^{vi}. (**g**) Ti vs. Fe^{vi}. (**h**) Ti vs. Mg^{vi}.

To highlight variations in shale-hosted V deposits and contribute to a more holistic deposit model, the geochemistry of the Van Property is compared to other shale-hosted V deposits (Figs. 6 to 9), which were selected based on V grade (>0.15 V_2O_5 wt%) and their reported major, minor, and trace element composition (Tables 2 and 3). The selected deposits are, from youngest to oldest: (1) Mecca Quarry Shale from Indiana and Illinois, U.S.A. (Coveney and Martin 1983; Peacor et al. 2000); (2) historical data from the Duo Lake Formation at the Van Property, Flat Lakes, NWT, Canada (Carne and Gish 1999); (3) Moss prospect, Yukon, Canada

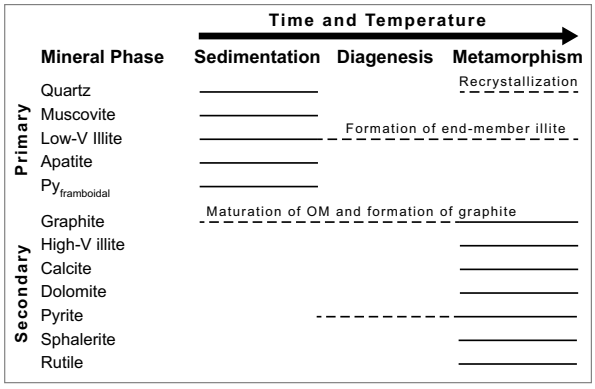

Figure 14. Paragenetic sequence based on mineralogical observations and analyses. See text for details.

(Gadd et al. 2019); (4) Storsjøn-Myrvikken in Jämtland, Sweden (Leventhal 1991); and (5) Zhongcun deposit, southern China (Fu et al. 2023). All these deposits are of Paleozoic age (early Cambrian to Pennsylvanian) and vary in host lithology, metamorphic grade, TOC and S concentrations, V-hosting minerals, and the reported process(es) responsible for V enrichment (Table 6 with listed references). Some of these features (e.g., age) are common for most known shale-hosted V deposits. In contrast, other characteristics (e.g., host lithology, content of TOC and S content, mineralogy) are much more variable than summarized in Kelley et al. (2017).

Within the selected deposits, host lithology is not restricted to black shales, marls, or mudstones (Kelley et al. 2017) and rather includes silica-rich, very fine-grained sedimentary rocks with a minor clay component such as the siliceous argillites observed at both the Van Property and Zhongcun deposits (Fig. 6a). Therefore, deposits show similar or higher than average V grades of the black shales and mudstones from the Mecca Quarry Shale, Moss prospect, and Storsjøn-Myrvikken (Fig. 7e; Tables 2–3). Hence, clay minerals, whose abundance exceeds 55% in shales (Shaw and Weaver 1965), are not solely responsible for scavenging and retaining V, although authigenic illite is commonly referred to as the dominant V host in shale-hosted V deposits (Coveney and Martin 1983; Meunier 1994; Peacor et al. 2000). Therefore, it seems, phases other than illite can contribute to the V budget of shale-hosted V deposits. Recent studies from Fu et al. (2023) and Yang et al. (2023) showed that V is also hosted in hydrothermally formed, V-rich micas (roscoelite, mannardite), anatase, and secondary goethite.

Most shale-hosted V deposits have average TOC contents exceeding 5 wt% (Kelley et al. 2017), with the exception of Moss (2.14 ± 1.69 wt%; Fig. 7c; Table 2). Although there is a positive linear correlation between TOC and V (Fig. 8e), suggesting organic matter plays a critical role in V enrichment (Lewan and Maynard 1982; Breit and Wanty 1991; Leventhal 1991), a direct relationship between high-TOC content and V enrichment is ambiguous because organic-rich shales such as the reference Devonian Ohio shale SDO-1 (Fig. 8e; Table 2) has relatively low metal, especially V, concentrations. Lu et al. (2021) showed that dissolved organic matter, V availability in seawater, and the redox state of bottom waters control V enrichment over time since V concentrations varied in stratigraphic horizons of the lower Cambrian Nuititang Formation,

Table 6. Summary of shale-hosted V deposits in comparison to data presented in this study from the Van Property

Deposit	Stratigraphy	Age	Lithology using $\log(SiO_2/Al_2O_3)$ after Herron (1988)	Metamorphic grade	V_2O_5 (wt%)	TOC (wt%)	V-bearing minerals	Process of metal enrichment
Mecca Quarry Shale, Illinois and Indiana, U.S.A. [1, 2]	Linton Formation, Carbondale Group	Pennsylvanian, Upper Carboniferous	Black shale	none	0.80 ± 0.53	28.8 ± 13.9	Authigenic illite, minor kerogen	Organic matter originated both from terrestrial (peat) and marine (algae?) source; V enrichment from low-*T* brines circulating through shales during diagenesis forming V-rich illite and adding V to kerogen
Van Property, NWT [3]	Duo Lake Formation, Road River Group	Lower Ordovician to Devonian	Siliceous argillite	(Sub-)greenschist	0.53 ± 0.17	7.85 ± 3.21	High-V illite, rutile, carbonaceous matter	V enrichment of carbonaceous matter during deposition in open system by metalation and formation of geoporphyrins; enrichment of V in high-V illite and rutile during late-stage metamorphism due to release of V as V^{3+} and VO^{2+} from degrading geoporphyrins
Van Property, NWT [4]	Duo Lake Formation, Road River Group	Lower Ordovician to Devonian	Siliceous argillite	(Sub-)greenschist	0.48 ± 0.18	6.89 ± 1.59	V-rich mica (roscoelite?), potentially asphaltene, sulvanite, corvusite (secondary)	V enrichment by hydrocarbon-rich, SEDEX-like hydrothermal fluid, whereas V was transported as organo-metallic complex; illite and organic matter became enriched in V upon contact of hydrothermal fluids with muds on seafloor; later diagenesis transformed V-rich illite to V-rich mica
Moss, YK [5]	Road River Group	Late Cambrian to Middle Devonian	Black shale to siliceous mudstone		0.23 ± 0.05	2.71 ± 0.63	NA	NA
Storsjøn-Myrvikken, Jämtland, SWE [6]	Alum Shale Formation	Cambrian	Siliceous mudstone	Low grade	0.36 ± 0.11	12.9 ± 0.85	Illite and/or organic matter	Secondary enrichment of V by metamorphically induced hydrothermal fluids originated from the basement; organic matter and pyrite acted as reductant
Zhongcun, CHI [7]	Shuigouku Formation	Early Cambrian	Siliceous mudstone to siliceous argillite	NA	1.28 ± 1.44	7.47 ± 4.78	Roscoelite, mannardite, V-bearing goethite, sulvanite, anatase	Scavenging of V from ambient seawater

Note: [1] Coveney and Martin (1983); [2] Peacor et al. (2000); [3] This study; [4] Carne and Gish (1999); [5] Gadd et al. (2019); [6] Leventhal (1991); [7] Fu et al. (2023).

South China. Hence, the occurrence of shale-hosted V deposits may not only be a function of TOC content but also how much V was dissolved in seawater at any given time in the geologic record.

The relationship between reduced S and V in shale-hosted V deposits is even less straightforward (Fig. 8d); S exceeds 1 wt% in most shale-hosted V deposits (Kelley et al. 2017). However, both the Van Property and Zhongcun deposits have S < 1 wt% (Table 2). It has long been assumed that H_2S is an effective reductant in shales converting oxidized, mobile V^{5+} to reduced, less mobile V^{4+} or V^{3+} (Breit and Wanty 1991; Wanty and Goldhaber 1992). However, the lack of correlation between S and the occurrence of V enrichment in deposits such as the Van Property with relatively low S indicates: (1) S does not play a critical role in V enrichment in shale-hosted deposits with S < 1 wt%, and (2) S is most likely introduced into shale-hosted deposits independently from V, for instance by an oxidized brine similar to fluids forming sedimentary exhalative deposits (e.g., Emsbo et al. 2016; Goodfellow and Lydon 2007). Although bacteria in mudstones and shales are common S producers via bacterial sulfate reduction of seawater (e.g., Canfield 2001) forming framboidal pyrite, this S source is interpreted to be minimal at the Van Property. Here, prismatic pyrite and sphalerite are not authigenic (Fig. 14) and show evidence that they were formed by a hydrothermal fluid that encountered the siliceous argillite of the OSD after diagenesis since sulfides have random orientation, occur with rutile (also secondary; Fig. 14), and overgrow the quartz-rich matrix (Figs. 5 and 11).

The positive correlations of V with other metals such as Mo, Ni, Zn, and Cu (Figs. 8e and 8g–8j) emphasize that V enrichment could be related to several processes: (1) syngenetic scavenging from seawater and enrichment in authigenic material coevally with Mo (e.g., Algeo and Maynard 2004; Tribovillard et al. 2012) and (2) (epigenetic) enrichment involving hydrothermal brines that also add Zn and/or Cu (e.g., Goodfellow and Lydon 2007; Hitzman et al. 2012; Brown 2014; Emsbo et al. 2016). The enrichment of V during sedimentation, diagenesis, or metamorphism in the selected deposits (Table 6 and cited references therein) is a function of host lithology, geologic setting, and most likely the metamorphic grade. McGill et al. (2024) showed that the depositional regime in which the V-enriched siliceous argillites formed was both anoxic and euxinic. The potential impact, especially of the latter, has so far not been sufficiently addressed in literature. It is, however, strongly assumed that metamorphism can contribute to V enrichment by liberation of V from carbonaceous matter due to the destruction of geoporphyrins in crude oils with increasing temperature (Lewan and Maynard 1982; Lewan 1984; Filby 1994; Greenwood et al. 2013). The role of metamorphism on V-bearing phases at the Van Property is discussed below in more detail.

Mineral hosts of vanadium

The mineralogy of V-hosting phases has been studied in organic-rich sedimentary rocks. Many workers identified inorganic phases as hosts, which are clays illite, mannardite, and roscoelite, and/or oxides rutile or anatase, karelianite, eskolaite, schreyerite, oxyvanite, unknown V-Ti-bearing oxides, and rare sulfides such sulvanite (Coveney and Martin 1983; Carne and Gish 1999; Peacor et al. 2000; Di Cecco et al. 2018; Lu et al. 2021; Veselovský et al. 2021; Fu et al. 2023; Yang et al. 2023). Additionally, organic matter has long been known to hold substantial amounts of V since crude oil and the kerogen and bitumen fractions of sedimentary rocks can be enriched in V (Fester et al. 1927; Hodgson 1954; Krauskopf 1955; Fischer et al. 1968; Vine and Tourtelot 1970; Mercer et al. 1992, 1993; Filby 1994).

The current study at the Van Property identified two inorganic phases hosting relatively high amounts of V: (1) high-V illite with up to 13 wt% V_2O_3, and (2) rutile with up to 4.4 wt% V_2O_5 (Fig. 11; Table 5). Although illite is a common V-host in shale-hosted deposits, two types occur at the Van Property (Figs. 11 and 12), of which only high-V illite is relatively enriched in vanadium (average = 10.26 ± 2.32 wt% V_2O_3, Fig. 13), has a composition close to I/S (i.e., K = 0.51 ± 0.03 apfu, Fig. 12), is apparently the 1*M* polytype (personal communication A. Zhang 2023), is closely associated with carbonaceous matter, and does not show any indication of deformation (i.e., kinking). This is similar to the study by Lu et al. (2021), who identified V-enriched illite as $1M/1M_d$ polytype, closely associated with pyrite and organic matter. However, in contrast to the study of Lu et al. (2021), the high-V illite at the Van Property does not show pyrite inclusions and a formation involving dissolved organic matter and illitization during diagenesis cannot be assumed. The correlation of V with several elements on various crystallographic sites (Fig. 13) rather indicates that V occurs in more than one oxidation state in high-V illite. The negative correlation of V^{3+} with Al^{3+} on the octahedral site is common in high-V illite and also observed both in low-V illite at the Van Property and in V-bearing authigenic illite from the Mecca Quarry shale, Indiana (Coveney and Martin 1983; Peacor et al. 2000). Vanadium on the tetrahedral site negatively correlates with Si^{4+} and positively with Al^{3+} (Figs. 13a and 13b). This could either be due to coupled substitution (i.e., $V^{5+} + Al^{3+} \leftrightarrow 2Si^{4+}$) or the occurrence of a vanadyl ion VO^{2+} on the tetrahedral site. Coupled substitution with V in the highly oxidized mobile state of V^{5+} (Breit and Wanty 1991; Wanty and Goldhaber 1992) has only been reported from synthetic illite in a hydrated environment (Wei et al. 1999) and is not seen as viable option due to the charge imbalance and ionic radii difference between Si^{4+} and V^{5+} of 0.26 and 0.355 Å, respectively (Shannon 1976), on the tetrahedral site. These charge and size differences would hinder effective substitution according to Goldschmidt's rules of cation substitution (Goldschmidt 1937). In contrast, the vanadyl ion is a common component in organic-rich shales and mudstones since it is formed by the process of metalation of organic matter (i.e., formation of metallo-organic complexes such as geoporphyrins) and which occurs in unconsolidated sediments prior to diagenesis (Lewan and Maynard 1982). During maturation of carbonaceous matter by diagenesis and/or metamorphism, geoporphyrins demetallate, releasing VO^{2+} (Lewan and Maynard 1982; Lewan 1984; Filby 1994), which then can be introduced into inorganic minerals. Yang et al. (2023) described the occurrence of VO^{2+} and V^{3+} in mannardite that formed in strongly reduced, euxinic shales. Although the origin of V^{3+} and VO^{2+} cannot be constrained in this study at the Van Property, a hydrothermal origin for V^{3+} and VO^{2+} is

less likely because the transport of VO^{2+} in hydrothermal fluids is restricted to relatively oxidized and acidic conditions (Lewan 1984; Breit and Wanty 1991; Wanty and Goldhaber 1992). Moreover, the solubilities of V^{3+} and VO^{2+} are limited in hydrothermal fluids (Wanty and Goldhaber 1992), and the amount of V occurring in the siliceous argillite at the Van Property could not be explained. As described below, a relatively Zn-rich, late-stage hydrothermal fluid was circulating through siliceous argillite, albeit the relative timing is unknown as of yet, depositing sphalerite (Figs. 5c, 5g, 5h, 11a, and 11h). It is unlikely that Zn and V were transported coevally since transport conditions (T, redox) differ between both metals. Moreover, the V concentration in sediment-hosted Zn deposits is not associated with hydrothermal activity but rather with scavenging from seawater or metamorphism (Canet et al. 2003; Paradis and Goodfellow 2012).

Rutile can have variable amounts of V that substitute for Ti^{4+} and, together with other V-bearing oxides such as karelianite, schreyerite, eskoalite, or oxyvanadite, have been reported in moderately metamorphosed shale deposits such as the Giant Green deposit, Madagascar (Di Cecco et al. 2018) and Chylin, Bohemian massif, Czech Republic (Veselovský et al. 2021). The vanadium content in rutile at the Van Property (1.13 ± 1.19 wt% V_2O_3) is lower than in rutile from the Green Giant deposit (2.88 ± 1.75 wt% V_2O_3; Di Cecco et al. 2018). We assume that the higher metamorphic grade (i.e., greenschist facies and higher) at both Green Giant and Chylin compared to the siliceous argillites at the Van Property resulted in a more complete breakdown of V-bearing clays and carbonaceous matter, resulting in the release of V, formation of rutile, and the subsequent incorporation of V^{4+} into metamorphic rutile (Di Cecco et al. 2018). Since the metamorphic grade at the Van Property was lower [i.e., sub-greenschist facies (Carne and Gish 1999; Flavelle 2013)], karelianite, eskoalite, schreyerite, or oxvanite did not form and the V content of rutile is lower. Further studies are, however, needed to confirm this assumption.

Although illite and rutile have been identified at the Van Property as V-bearing phases, it was tested to determine if they can contribute all of the bulk V. The following mass-balance calculation was applied:

$$\Sigma V = a \times P_1 + b \times P_2 + c \times P_n + \ldots \quad (1)$$

in which a, b, and c are the fractional abundances of V in minerals and P_1, P_2, P_n are abundances of the V-bearing mineral phases identified by XRD (e.g., illite, rutile). Table 7 summarizes the results for V-bearing samples that were analyzed by both lithogeochemistry and EMPA (i.e., hf05-33, -34, -36, -37) and using different proportions of low-V to high-V illite (i.e., 30:70 to 80:20). The calculations reveal that illite and rutile alone, and independent of the proportion of low-V illite to high-V illite, cannot account for the bulk V concentration. Both phases can contribute only between 9–59% of the bulk V (Table 7), implying that at least one more phase must host a significant fraction of total V. Of the identified phases present in the samples, the most likely one is carbonaceous matter.

Although no spectroscopic or chromatographic analyses were performed to either identify if organic carbonaceous matter

Table 7. Mass-balance calculation involving illite and rutile and list of V resources in crude oil, bitumen, and kerogen from selected locations

Sample No.	Bulk composition			Low-V illite[b]		High-V illite[b]		Rutile[b]		Calculated total composition			Unaccounted V [to be hosted by other phase(s)][c]	
	V (ppm)	V_2O_5 (wt%)	Illite (wt%)	Ratio[a]	a	P_1 (ppm)	b	P_2 (ppm)	c	P_3 (ppm)	V (ppm)	V_2O_5 (wt%)	Of bulk (%)	V (ppm)	V_2O_5 (wt%)
hf05-33	3870	0.69	1.7	30:70	0.005	5292	0.012	69 744	0.004	11 317	**920**	**0.16**	**23**	2968	0.53
	3870	0.69		50:50	0.009	5292	0.009	69 744	0.004	11 317	**683**	**0.12**	**18**	3187	0.57
	3870	0.69		80:20	0.014	5292	0.003	69 744	0.004	11 317	**354**	**0.06**	**9**	3516	0.63
hf05-34	3610	0.64	1.7	30:70	0.005	5292	0.012	69 744	0.004	11 317	**920**	**0.16**	**25**	2708	0.48
	3610	0.64		50:50	0.009	5292	0.009	69 744	0.004	11 317	**683**	**0.12**	**19**	2927	0.52
	3610	0.64		80:20	0.014	5292	0.003	69 744	0.004	11 317	**354**	**0.06**	**10**	3256	0.58
hf05-36	1380	0.25	1.5	30:70	0.005	5292	0.011	69 744	0.004	11 317	**817**	**0.15**	**58**	579	0.10
	1380	0.25		50:50	0.008	5292	0.008	69 744	0.004	11 317	**608**	**0.11**	**44**	772	0.14
	1380	0.25		80:20	0.012	5292	0.003	69 744	0.004	11 317	**294**	**0.05**	**23**	1062	0.19
hf05-37	3130	0.56	1.6	30:70	0.005	5292	0.011	69 744	0.004	11 317	**871**	**0.16**	**27**	2277	0.41
	3130	0.56		50:50	0.009	5292	0.008	69 744	0.004	11 317	**648**	**0.12**	**21**	2482	0.44
	3130	0.56		80:20	0.014	5292	0.003	69 744	0.004	11 317	**340**	**0.06**	**11**	2790	0.50

Notes: Composition of V in selected crude oils and bitumen is listed below table to highlight carbonaceous matter as a likely source for V at the Van Property.

[a] Ratio between low-V illite and high-V illite. No quantitative assessment was done to quantify the ratio and low-V illite dominates based on observations. However, the range of ratios depicts realistic scenarios.

[b] Mass-balance calculation using Equation 1: $\Sigma V = a \times P_1 + b \times P_2 + c \times P_n + \ldots$ where a, b, and c are the decimal proportions of low-V illite, high-V illite, and rutile for each sample based on XRD results, and P1, P2, P3 are the average V content in low-V illite, high-V illite, and rutile in ppm based on EMPA results.

[c] V content reported from crude oils and bitumen as potential third host for V: Heavy bio-degraded marine oil; Boscan, Venezuela (Cretaceous) with 1200 ppm (Mercer et al. 1992), Bitumen, New Albany shale, Indiana (marine, Mississippi-Devonian) with 2700 ppm (Mercer et al. 1992) and Crude oil, Boscan, Venezuela (Cretaceous) with 4958 ppm (Chirinos et al. 2013).

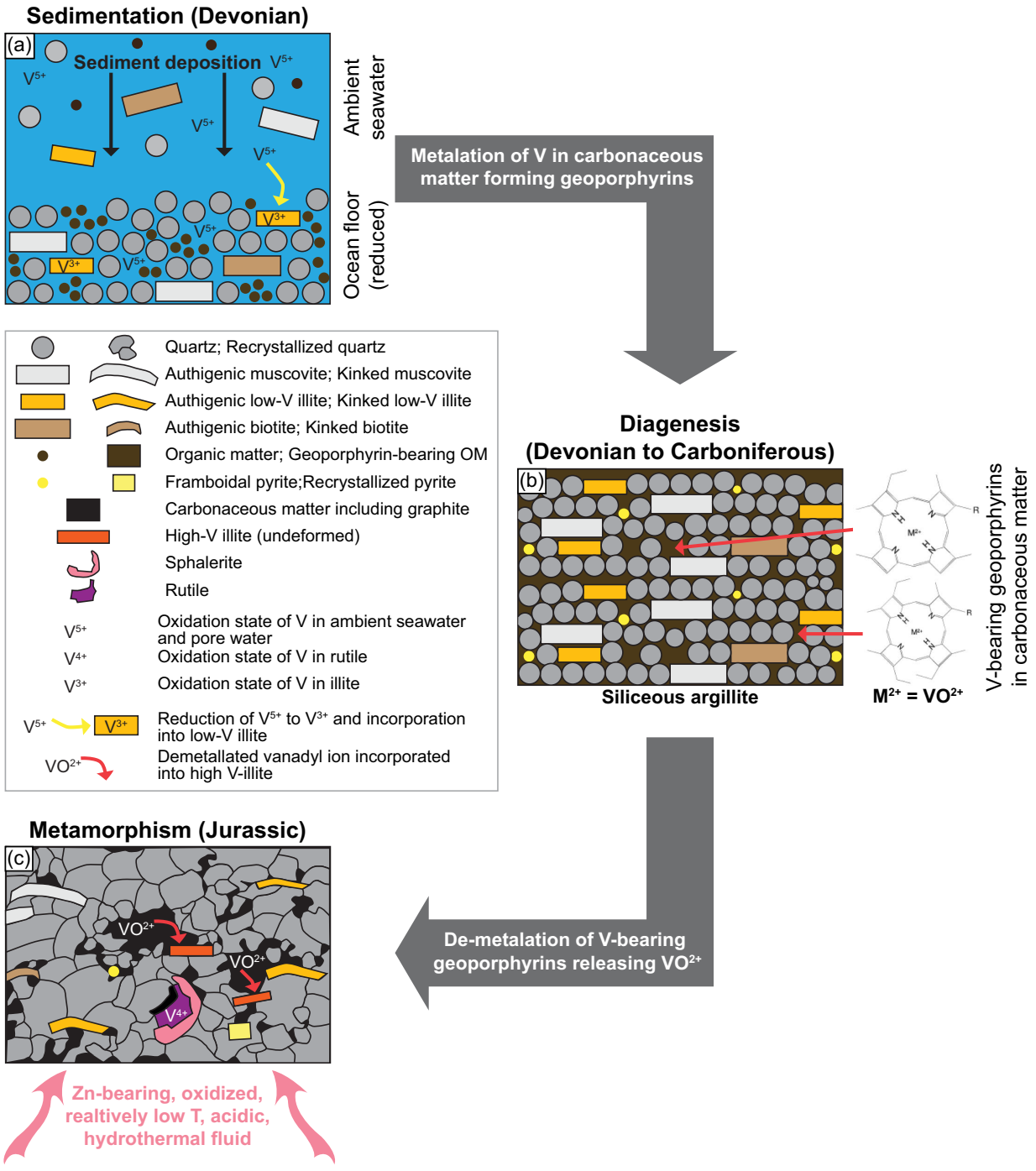

Figure 15. Simplified genetic model of V enrichment at the Van Property. (**a**) Sedimentation during Lower Devonian, (**b**) diagenesis during Devonian-Carboniferous, (**c**) metamorphism during Jurassic.

is present and to determine if it hosts V, the V concentration of crude oil, bitumen, and kerogen can reach several thousands of parts per million (Mercer et al. 1992; Chirinos et al. 2013). Furthermore, the positive correlation between V and TOC for siliceous argillites from the Van Property (Fig. 8c) indicates a strong role of total organic carbon in vanadium uptake. Although XRD identified graphite (Fig. 10) as the only carbonaceous phase, which is consistent with the degradation of organic matter under metamorphic conditions (Buseck and Huang 1985), Costantinides et al. (1959) and Lewan (1980, 1984) stated that V-bearing geoporphyrins in kerogen and bitumen do not fully demetallate (e.g., lose V-bearing organo-metallic complexes and form inorganic complexes such as VO^{2+}) at temperatures in excess of 300–350 °C in crude oils. Peacor et al. (2000)

showed that kerogen is an important host of V in the weekly metamorphosed black shales of the Mecca Quarry, Indiana. This finding supports the occurrence of V with carbonaceous matter at siliceous argillite (OSD) at the Van Property.

Process of vanadium enrichment at the Van Property

The model for the enrichment of V in shales or siliceous argillites must consider the age, depositional environment, lithological composition, mineralogy of V-hosted phases, amount of carbonaceous matter, and metamorphic grade. Currently, there are several explanations of how V is enriched in shale-hosted V deposits: (1) oxidized V^{5+} is scavenged from ambient seawater by organic matter or clays in anoxic or euxinic basins and incorporated in illite as reduced V^{3+} and/or in organic matter as V^{4+} (Breit and Wanty 1991) upon deposition or during late diagenesis, forming the additional V-bearing phases roscoelite, mannardite, or anatase (Fu et al. 2023); (2) V is scavenged directly from ambient seawater by dissolved organic matter of nano-size that then accumulated in shale and was taken up by smectite forming V-bearing smectite-nano-composites. During diagenesis, illitization of smectite and pyrolysis (i.e., maturation of organic matter) of organic matter results in V release and uptake of V^{3+} into illite (Lu et al. 2021); (3) low-T, hydrothermal brines circulated through sediments during deposition and early diagenesis forming V-rich, authigenic illite and V-rich organic matter (Peacor et al. 2000); (4) hydrothermal fluids containing immiscible, V-bearing petroleum droplets circulated through unconsolidated, organic-rich seafloor sediments and V^{3+} was incorporated into illite and organic matter. Diagenesis transferred V-bearing illite into roscoelite (Carne and Gish 1999). Alternatively, a petroleum ore fluid was the preferred transport medium for metals including V in shale-hosted deposits (Emsbo et al. 2009); and (5) secondary, supergene enrichment may further upgrade the V content in shales due to the circulation of meteoric fluids through V-enriched shales, forming V-rich goethite (Fu et al. 2023).

At the Van Property, processes 2 to 5 are dismissed as the dominant explanations of V enrichment. Fu et al. (2023) described the occurrence of micro-sized pyrite inclusions in illite-organic nanocomposites formed by dissolved organic matter that scavenged V from ambient seawater, were incorporated into smectite upon deposition and then into illite upon subsequent illitization of smectite. Although pyrite inclusions were observed in some illite, they only occur in low-V illite (Figs. 5e and 11h). Formation by syn-genetic and syn-diagenetic hydrothermal fluids that carried V either in a hydrothermal fluid (Peacor et al. 2000) or in immiscible petroleum droplets (Carne and Gish 1999; Emsbo et al. 2009) is also excluded for these reasons: (1) solubility of V in hydrothermal fluids is very low and cannot explain the amount of V present at the Van Property (Breit and Wanty 1991); (2) the amount of V held in the carbonaceous fraction is at least 40% (Table 7) and cannot be explained by minor petroleum droplets in a hydrothermal fluid. Although the source of the carbonaceous matter (e.g., primary: source rock or secondary: trap; Filby 1994, and references therein) cannot be constrained in this study, it is a major V source in which V became enriched either upon deposition and/or diagenesis in the two upper members of the OSD; (3) the occurrence of V is stratigraphically limited to the Lower Cherty Mudstone Member and the upper part of the Upper Siliceous Mudstone Member (Fig. 3). Any petroleum fluid flow also should have impacted the underlying members of the OSD (i.e., Calcareous Mudstone Member, Siliceous Mudstone Member, Transition Member) if there were a permeable pathway for petroleum fluids. However, these units are several tens to hundreds of meters thick and consist of less permeable, fine-grained siliciclastic lithologies (Carne and Gish 1999).

Additionally, only the upper part of the Upper Cherty Mudstone Member shows V enrichment (Carne and Gish 1999), whereas the remaining member has low-V content. This selective enrichment within the same stratigraphic horizon is difficult to explain by a circulating petroleum ore fluid that also enriched the older, conformably underlain Lower Siliceous Mudstone Member; (4) high-V illite and rutile formed during or after low-grade metamorphism and incorporated V either as V^{3+}, V^{4+}, or VO^{2+} in their crystal structure. Vanadium most likely originated from the degradation of carbonaceous matter and demetallation of geoporphyrins. Furthermore, the close spatial occurrence of high-V illite and rutile with randomly oriented pyrite and sphalerite and the strong positive correlation of V with Zn suggest that a low-T, Zn-bearing hydrothermal fluid circulated through the argillite; and (5) although Carne and Gish (1999) described the occurrence of secondary corvusite on weathered surfaces at the Janice and James Creek showings, this was not observed in the studied samples and hence, the role of supergene processes is minimal or even absent.

Based on the lithogeochemical and mineralogical results in this study, the enrichment and incorporation of V in various mineral phases in the siliceous argillite of the OSD at the Van Property occurred via different processes (Fig. 15). First, upon the deposition of quartz-rich, fine-grained sediments and organic matter under anoxic conditions and beneath the calcite compensation depth (Turner et al. 2011) in the Lower Devonian, V was incorporated as a trace component into low-V illite and formed geoporphyrins via metalation in carbonaceous matter during early diagenesis (Figs. 15a and 15b). The likely source of V was V^{5+} or V^{4+} scavenged either from ambient seawater [illite formation (Breit and Wanty 1991)] or pore water interacting with carbonaceous matter (Lewan 1980; Lewan and Maynard 1982; Filby 1994) where an open system was crucial for effective large-scale V scavenging (Lewan and Maynard 1982). During diagenesis, lithification of argillite occurred, as well as maturation of low-V illite to illite end-member composition (i.e., illite with $K = 0.80–0.88$ apfu) and maturation of carbonaceous matter (Fig. 15b). Furthermore, during (sub-)greenschist metamorphism, quartz and low-V illite deformed, the carbonaceous material transformed to graphite, and geoporphyrins demetallated (Fig. 15c). Lastly, a low-T, Zn-rich hydrothermal fluid circulated through siliceous argillite forming hydrothermal illite of I/S composition in which V was enriched (Fig. 15c). Due to the two oxidation states of V present in high-V illite (i.e., V^{3+} and V^{4+} in VO^{2+}), we propose that vanadyl ions formed by demetallation of geoporphyrins were incorporated into a later generation of high-V illite during metamorphism. Further studies on high-V illite using transmission electron microscopy and atom probe tomography

will be utilized to confirm this. The timing of the Zn-rich hydrothermal fluid is unknown and may be related to metamorphism during the Jurassic (i.e., a late metamorphic fluid) or intrusive activity that formed the nearby Cantung tungsten deposit in the Cretaceous (Ootes et al. 2013).

Implications

This study investigated the enrichment of V at the Van Property, Northwest Territories, using lithogeochemistry, SEM, XRD, and EMPA. The results show that: (1) V enrichment is not restricted to shale; (2) high-V illite, rutile, and assumingly carbonaceous matter are the predominant V hosts; and (3) the genesis is a complex interplay of syngenetic (e.g., V scavenging from seawater), diagenetic (e.g., metalation of V forming organo-complexes), and metamorphic (e.g., release of V due to de-metalation; hydrothermal fluid interaction) processes. These results have implications on both the role of metamorphism regarding V enrichment and exploration for shale-hosted V deposits. The former is not well constrained yet, and this study provides insight into how metamorphism can refine metal enrichment and the relationship of V uptake by both inorganic and organic phases during syngenetic, diagenetic, and metamorphic conditions. Vanadium has an increasing demand, and shale-hosted deposits are a viable yet under-exploited option. Results from this study aid in refining the current deposit model by incorporating variations in host lithogeochemistry and mineralogy and the role of metamorphism and, hence, target potential V prospects in metamorphosed Paleozoic sedimentary basins that have not yet been considered for exploration.

Acknowledgments and Funding

The authors thank the team of Chris Gunning and Adrian Zhang at SGS for XRD analyses and discussions on the results. Ravi Sidhu (Manitoba Institute of Materials, University of Manitoba) and Panseok Yang (Department of Earth Sciences, University of Manitoba) are thanked for their support at SEM and EMPA, respectively. S.M.B. thanks Michael Gadd for providing a detailed data set on the Moss prospect for this study. The authors appreciate the insightful review of an anonymous reviewer and Maria Boni, which improved the manuscript. We thank Associate Editor Denis Fougerouse for handling the paper. The study was funded by the Northwest Territories Geological Survey and an NSERC Discovery grant RGPIN-2022-04118 awarded to S.M.B. This is MERC publication number MERC-2024-02.

References Cited

Aitken, J.D. and Cook, D.G. (1974) Effect of antecedent faults on “Laramide” structure, Mackenzie arc. Report of Activities, part B, November 1973 to March 1974, Paper 74-01B, 259–264. Geological Survey of Canada.

Aja, S.U. (1989) A hydrothermal study of illite stability relationships between 25 and 250 °C and Pv 1/4 PH2O. Ph.D. thesis, Washington State University.

Aja, S.U. (2020) On the thermodynamic stability of illite and I-S minerals. Clays and Clay Minerals, 67, 518–536.

Algeo, T.J. and Maynard, J.B. (2004) Trace-element behavior and redox facies in core shales of Upper Pennsylvanian Kansas-type cyclothems. Chemical Geology, 206, 289–318.

Becker, A. (1995) Quartz pressure solution: Influence of crystallographic orientation. Journal of Structural Geology, 17, 1395–1405.

Boni, M., Bouabdellah, M., Boukirou, W., Putzolu, F., and Mondillo, N. (2023) Vanadium ore resources of the African continent: State of the Art. Ore Geology Reviews, 157, 105423.

Breit, G.N. and Wanty, R.B. (1991) Vanadium accumulation in carbonaceous rocks: A review of geochemical controls during deposition and diagenesis. Chemical Geology, 91, 83–97.

Brigatti, M.F., Caprilli, E., Marchesini, M., and Poppi, L. (2003) The crystal structure of Roscoelite-1M. Clays and Clay Minerals, 51, 301–308.

Brown, A.C. (2014) Low-temperature sediment-hosted copper deposits. In S.D. Scott, Ed., Treatise on Geochemistry, 13, p. 251–271. Elsevier.

Buseck, P.R. and Huang, B.-J. (1985) Conversion of carbonaceous material to graphite during metamorphism. Geochimica et Cosmochimica Acta, 49, 2003–2016.

Canet, C., Alfonso, P., Melgarejo, J.C., and Jorge, S. (2003) V-rich minerals in contact-metamorphosed Silurian sedex deposits in the Poblet Area, Southwestern Catalonia, Spain. Canadian Mineralogist, 41, 561–579.

Canfield, D.E. (2001) Biogeochemistry of sulfur isotopes. Reviews in Mineralogy and Geochemistry, 43, 607–636.

Carne, R.C. and Gish, R.F. (1999) Assessment Report describing Geological and Geochemical Surveys on the Van 1 Claim; private report, Nordac Resources Ltd.

Cecile, M.P. (1982) The Lower Paleozoic Misty Creek Embayment, Selwyn Basin, Yukon and Northwest Territories, 78 p. Geological Survey of Canada.

Chirinos, J., Oropeza, D., González, J., Ranaudo, M., and Russo, R.E. (2013) Determination of vanadium/nickel proportionality in the asphaltene fraction of crude oil using thin-layer chromatography with femtosecond laser ablation-inductively coupled plasma-mass spectrometry. Energy & Fuels, 27, 2431–2436.

Costantinides, G., Arich, G., and Lomi, C. (1959) Detection and behaviour of porphyrin aggregates in petroleum residues and bitumens. 5th World Petroleum Congress, New York, U.S.A., Paper WPC-8411.

Coveney, R.M. and Martin, S.P. (1983) Molybdenum and other heavy metals of the Mecca Quarry and Logan Quarry shales. Economic Geology and the Bulletin of the Society of Economic Geologists, 78, 132–149.

Dewing, K., Sharp, R.J., Ootes, L., Turner, E.C., and Gleeson, S. (2006) Geologic assessment of known Zn-Pb showings, Mackenzie Mountains, Northwest Territories. Current Research, 2006–A4, 12.

Di Cecco, V.E., Tait, K.T., Spooner, E.T.C., and Scherba, C. (2018) The vanadium-bearing oxide minerals of the Green Giant Vanadium-graphite Deposit, Southwest Madagascar. Canadian Mineralogist, 56, 247–257.

Dixon, J. (1999) Mesozoic-Cenozoic stratigraphy of the northern Interior Plains and Plateau, Northwest Territories. Geological Survey of Canada. Bulletin, 536, 56.

Eisbacher, G.H. (1981) Sedimentary tectonics and glacial record in the Windermere Supergroup, Mackenzie Mountains, northwestern Canada, Paper 80-27, 40 p. Geological Survey of Canada.

Elbokl, T. (2022) Is V the new Li? Canadian Mining Journal The Northern Miner Group.

Emsbo, P., Williams-Jones, A.E., Koenig, A.E., and Wilson, S.A. (2009) Petroleum as an agent of metal transport: Metallogenesis and exploration implications. In P.A. Williams, Ed., Proceedings of the Tenth Biennial SGA Meeting, p. 99–101. James Cook University, Townsville, Queensland, Australia.

Emsbo, P., Seal, R.R., Breit, G.N., Diehl, S.F., and Shah, A.K. (2016) Sedimentary exhalative (sedex) zinc-lead-silver deposit model. U.S. Geological Survey Scientific Investigations Report 2010-5070-N, 57 p. U.S. Geological Survey.

European Commission (2020) Critical Raw Materials Resilience: Charting a Path towards greater Security and Sustainability. Communication from the Commission to the European Parliament, the Council, the European Economic and Social Committee and the Committee of the Regions, #474. European Commission.

Fester, G.A., Bertuzzi, F., and Gitlin, J. (1927) Bituminous materials from the Republic of Argentina: 1. Bitumen of the rafaelites; 2. Vanadium in the rafaelites; 3. Bitumen in the lignites of the Republic of Argentina. Academia Nacional de Ciencias Boletin. Cordoba. Argentine Republic, 30, 117–122.

Filby, R.H. (1994) Origin and nature of trace element species in crude oils, bitumens and kerogens: Implications for correlation and other geochemical studies. Geological Society of London Special Publications, 78, 203–219.

Fischer, R.P. (1968) The uranium and vanadium deposits of the Colorado Plateau region. In J.D. Ridge, Ed., Ore deposits of the United States, 1, 735–746. American Institute of Mining, Metallurgical, and Petroleum Engineers.

Fischer, R.P. (1975) Vanadium resources in titaniferous magnetite deposits. Geology and Resources of Vanadium Deposits. USGS Professional Paper 926-B, 10 p.

Fischer, R.P. and Stewart, J.H. (1961) Copper, vanadium, and uranium deposits in sandstone; their distribution and geochemical cycles. Economic Geology and the Bulletin of the Society of Economic Geologists, 56, 509–520.

Fischer, R.P., Ohl, J.P., and Brien, H. (1968) Bibliography of the Geology and Resources of Vanadium to 1968. Geological Survey Bulletin, 1316, 168 p. U.S. Geological Survey.

Flavelle, E. (2013) Assessment Report describing Geochemical Sampling, Prospecting, Geological Mapping and Metallurgical Testing at the Van Property, 35 p. Strategic Metals Ltd.

Fu, X., Xu, L., Yan, H., Ye, H., and Ding, J. (2023) Mineralogy and trace element geochemistry of the early Cambrian black shale-hosted Zhongcun vanadium deposit, southern Qinling, China. Ore Geology Reviews, 155, 105371.

Gadd, M.G., Peter, J.M., Fraser, T., and Layton-Matthews, D. (2019) Lithogeochemical and sulphur isotope indicators of environment of formation and genesis of the Moss hyper-enriched black shale showing, Yukon. In N. Rogers, Ed., Targeted Geoscience Initiative: 2018 Report of Activities, Open File 8549, 163–178. Geological Survey of Canada.

Goldschmidt, V.M. (1937) The principles of distribution of chemical elements in minerals and rocks. Journal of the Chemical Society, 1937, 655–673.

Goodfellow, W.D. and Lydon, J.W. (2007) Sedimentary exhalative (SEDEX) deposits. In W.D. Goodfellow, Ed., Mineral Deposits of Canada: A Synthesis of Major Deposit Types, District Metallogeny, the Evolution of Geological Provinces, and Exploration Methods, Special Publication No. 5, 163–183. Geological Association of Canada, Mineral Deposits Division.

Gordey, S.P. (1988) Devono-Mississippian clastic sedimentation and tectonism in the Canadian Cordilleran miogeocline. In N.J. McMillan, A.F. Embry, and D.J. Glass, Eds. Devonian of the World: Proceedings of the Second International Symposium on the Devonian System, Memoir 14, p. 1–14. Canadian Society of Petroleum Geologists.

Gordey, S.P. and Anderson, R.G. (1993) Evolution of the northern Cordilleran miogeocline, Nahanni map area (105I), Yukon and Northwest Territories. Memoir, 428, 214 p. Geological Survey of Canada.

Gordey, S.P. and Roots, C.F. (2011) Regional setting. In E. Martel, E.C. Turner, and B.J. Fischer, Eds. Geology of the central Mackenzie Mountains of the northern Canadian Cordillera, Sekwi Mountain (105P), Mount Eduni (106A), and northwestern Wrigley Lake (95M) map-areas, Northwest Territories, NWT Special Volume 1, p. 18–30. Northwest Territories Geological Survey.

Gordey, S.P., Macdonald, J.D., Turner, E.C., and Long, D.G.F. (2011) Structural geology of the Central Mackenzie Mountains. In E. Martel, E.C. Turner, and B.J. Fischer, Eds., Geology of the Central Mackenzie Mountains of the Northern Canadian Cordillera, Sekwi Mountain (105P), Mount Eduni (106A), and Northwestern Wrigley Lake (95M) Map-Areas, Northwest Territories, NWT Special Volume 1, p. 215–250. Northwest Territories Geological Survey.

Greenwood, P.F., Brocks, J.J., Grice, K., Schwark, L., Jaraula, C.M.B., Dick, J.M., and Evans, K.A. (2013) Organic geochemistry and mineralogy. I. Characterisation of organic matter associated with metal deposits. Ore Geology Reviews, 50, 1–27.

Herron, M.M. (1988) Geochemical classification of terrigenous sands and shales from core or log data. SEPM Journal of Sedimentary Research, 58, 820–829.

Hitzman, M.W., Broughton, D., Selley, D., Woodhead, J., Wood, D., and Bull, S. (2012) The Central African Copperbelt. In J.W. Hedenquist, M. Harris, and F. Camus, Eds., Geology and Genesis of Major Copper Deposits and Districts of the World: A Tribute to Richard H. Sillitoe, Special Publication No. 16, 487–514. Society of Economic Geologists.

Hodgson, G.W. (1954) Vanadium, nickel, and iron trace metals in crude oils of Western Canada. AAPG Bulletin, 38, 2537–2554.

Huyck, H.L.O. (1991) When is a metalliferous black shale not a black shale? In R.I. Grauch and H.L.O. Huyck, Eds., Metalliferous Black Shales and Related Ore Deposits-Proceedings, 1989 United States Working Group meeting, International Geological Correlation Program Project 254, Circular 1058, 42–56. U.S. Geological Survey.

IMA (2021) The New IMA List of Minerals. International Mineralogical Association.

Jochum, K.P., Nohl, U., Herwig, K., Lammel, E., Stoll, B., and Hofmann, A.W. (2005) GeoReM: A new geochemical database for reference materials and isotopic standards. Geostandards and Geoanalytical Research, 29, 333–338.

Jowitt, S.M., Mudd, G.M., Werner, T.T., Weng, Z., Barkoff, D.W., and McCaffrey, D. (2018) The critical metals: An overview and opportunities and concerns for the future. In A.M. Arribas and J.L. Mauk, Eds., Metals, Minerals, and Society Special Publications No. 21, 25–38. Society of Economic Geologists.

Kelley, K.D., Scott, C.T., Polyak, D.E., and Kimball, B.E. (2017) Vanadium. In K.J. Schulz, J.H. DeYoung Jr., R.R. Seal, II, and D.C. Bradley, Eds., Critical Mineral Resources of the United States—Economic and Environmental Geology and Prospects for Future Supply, Professional Paper 1802, U1–U36. U.S. Geological Survey.

Krauskopf, K.B. (1955) Sedimentary deposits of rare metals. Economic Geology, 50th Anniversary Volume 1905–1955, 411–463.

Lawrence, M.G., Greig, A., Collerson, K.D., and Kamber, B.S. (2006) Rare earth element and yttrium variability in South East Queensland waterways. Aquatic Geochemistry, 12, 39–72.

Leventhal, J.S. (1991) Comparison of organic geochemistry and metal enrichment in two black shales: Cambrian alum shale of Sweden and Devonian Chattanooga Shale of United States. Mineralium Deposita, 26, 104–112.

Lewan, M.D. (1980) Geochemistry of vanadium and nickel in organic matter of sedimentary rocks. Ph.D. thesis, University of Cincinnati.

Lewan, M.D. (1984) Factors controlling the proportionality of vanadium to nickel in crude oils. Geochimica et Cosmochimica Acta, 48, 2231–2238.

Lewan, M.D. and Maynard, J.B. (1982) Factors controlling enrichment of vanadium and nickel in the bitumen of organic sedimentary rocks. Geochimica et Cosmochimica Acta, 46, 2547–2560.

Li, W., Ma, C., Gong, W., and Zhu, X. (2021) Clean production technology for effective recovery of vanadium from shale: Interaction between activators and vanadium-loaded minerals. Journal of Cleaner Production, 315, 128170.

Long, D.G.F. and Turner, E.C. (2012) Formal definition of the Neoproterozoic Mackenzie Mountains Supergroup (Northwest Territories), and formal stratigraphic nomenclature for terrigenous clastic units of the Katherine Group, Open File 7112, 40. Geological Survey of Canada.

Long, D.G.F., Rainbird, R.H., Turner, E.C., and MacNaughton, R.B. (2008) Early Neoproterozoic strata (Sequence B) of mainland northern Canada and Victoria and Banks islands: A contribution to the Geological Atlas of Northern Canadian Mainland Sedimentary Basin, Open File 5700, 27. Geological Survey of Canada.

Longridge, L. and Martinez, A. (2020) Lac Doré Project, Chibougamau, Québec, Canada: NI 43–101 Technical Report, Report No: R441.2020, 105 p. CSA Global.

Lu, Z., Hu, R., Han, T., Wen, H., Mo, B., and Algeo, T.J. (2021) Control of V accumulation in organic-rich shales by clay-organic nanocomposites. Chemical Geology, 567, 120100.

Maier, W.D., Barnes, S.J., and Groves, D.I. (2012) The Bushveld Complex, South Africa: Formation of platinum-palladium, chrome- and vanadium-rich layers via hydrodynamic sorting of a mobilized cumulate slurry in a large, relatively slowly cooling, subsiding magma chamber. Mineralium Deposita, 48, 1–56.

Mair, J.L., Hart, C.J.R., and Stephens, J.R. (2006) Deformation history of the northwestern Selwyn Basin, Yukon, Canada: Implications for orogen evolution and mid-Cretaceous magmatism. Geological Society of America Bulletin, 118, 304–323.

Martel, E., Turner, E.C., and Fischer, B.J. (2011) Geology of the central Mackenzie Mountains of the northern Canadian Cordillera, Sekwi Mountain (105P), Mount Eduni (106A), and northwestern Wrigley Lake (95M) map-areas, Northwest Territories. In E. Martel, E.C. Turner, and B.J. Fischer, Eds., Northwest Territories Geoscience Office Special Volume 1, 423 p. Northwest Territories Science Office.

McGill, D.A., Gregory, D.D., Reynolds, M.A., Concepcion, D.B., Martin, A.N., Schuth, S., and Brueckner, S.M. (2024) Geology and Geochemistry of the shale-hosted vanadium mineralization at the Van Property, Northwest Territories, Canada. Economic Geology and the Bulletin of the Society of Economic Geologists, in press.

McLennan, S.M. (1989) Rare earth elements in sedimentary rocks: Influence of provenance and sedimentary processes. Reviews in Mineralogy and Geochemistry, 21, 169–200.

Mercer, G.E., Regner, A.J., and Filby, R.H. (1992) Trace element distributions in kerogen, bitumen and pyrolysates isolated from the New Albany Shale. Preprints American Chemical Society Division of Fuel Chemistry, 37, 1761–1768.

Mercer, G.E., Fitzgerald, S., Day, J., and Filby, R.H. (1993) Determination of organic/inorganic associations of trace elements in kerogen of the New Albany shale. Fuel, 72, 1187–1195.

Meunier, J.D. (1994) The composition and origin of vanadium-rich clay-minerals in Colorado Plateau Jurassic sandstones. Clays and Clay Minerals, 42, 391–401.

Meunier, A. and Velde, B. (1989) Solid solutions in I/S mixed-layer minerals and illite. American Mineralogist, 74, 1106–1112.

Morris, G.A. and Nesbitt, B.E. (1998) Geology and timing of paleohydrogeological events in the Mackenzie Mountains, Northwest Territories, Canada. In J. Parnell, Ed., Dating and Duration of Fluid Flow and Fluid-Rock Interaction, Special Publication 144, 161–172. Geological Society.

Narbonne, G. and Aitken, J. (1995) Neoproterozoic of the Mackenzie Mountains, northwestern Canada. Precambrian Research, 73, 101–121.

Natural Resources Canada (2020) Critical Minerals in Canada. Natural Resources Canada.

Nelson, J.L., Colpron, M., and Israel, S. (2013) The Cordillera of British Columbia, Yukon, and Alaska. In M. Colpron, T. Bissig, B.G. Rusk, and J.F.H. Thompson, Eds., Tectonics, Metallogeny, and Discovery: The North American Cordillera and Similar Accretionary Settings, Special Publication, No. 17, 53–109. The Society of Economic Geologists.

Newman, A.C.D. and Brown, G. (1987) The chemical constitution of clays. In A.C.D. Newman, Ed., Chemistry of Clays and Clay Minerals, Monograph No. 6, 1–128. Longman Scientific and Technical.

Nozaki, Y. (2008) Rare earth elements and their isotopes in the ocean. In K.K. Turekian, Ed., Marine Chemistry and Geochemistry, 2nd ed., p. 39–51. Elsevier.

Ootes, L., Gleeson, S.A., Turner, E., Rasmussen, K., Gordey, S., Falck, H., Martel, E., and Pierce, K. (2013) Metallogenic evolution of the Mackenzie and Eastern Selwyn Mountains of Canada's Northern Cordillera, Northwest Territories: A compilation and review. Geoscience Canada, 40, 40–69.

Paradis, S. and Goodfellow, W. (2012) SEDEX deposits in the Cordillera: Current concepts on their geology, genesis, and exploration. A Targeted Geoscience Initiatives 3 and 4 Contribution, Open File 7144. Geological Survey of Canada.

Peacor, D.R., Coveney, R.M. Jr., and Zhao, G. (2000) Authigenic illite and organic matter: The principal hosts of vanadium in the Mecca Quarry Shale at Velpen, Indiana. Clays and Clay Minerals, 48, 311–316.

Pyle, L. and Jones, A.L. (2009) Regional geoscience studies and petroleum potential, Peel Plateau and Plain, Northwest Territories and Yukon, Open File 2009-02, 549 p. Northwest Territories Geoscience Office.

Rainbird, R.H., Jefferson, C.W., and Young, G.M. (1996) The early Neoproterozoic sedimentary Succession B of northwestern Laurentia: Correlations and paleogeographic significance. Geological Society of America Bulletin, 108, 454–470.

Rieder, M., Cavazzini, G., D'yakonov, Y.S., Frank-Kamenetskii, V.A., Gottardi, G., Guggenheim, S., Koval', P.W., Müller, G., Neiva, A.M.R., Radoslovich, E.W., and others. (1998) Nomenclature of the micas. Clays and Clay Minerals, 46, 586–595.

Rosenberg, P.E. (2002) The nature, formation, and stability of end-member illite: A hypothesis. American Mineralogist, 87, 103–107.

Schulz, K.J., DeYoung, J.H. Jr., Bradley, D.C., and Seal, R.R. II (2017) Critical mineral resources of the United States—An introduction. In K.J. Schulz, J.H. DeYoung Jr., R.R. Seal, II, and D.C. Bradley, Eds., Critical Mineral Resources of the United States—Economic and Environmental Geology and Prospects for Future Supply, Professional Paper 1802, A1–A14. U.S. Geological Survey.

Shannon, R.D. (1976) Revised effective ionic-radii and systematic studies of interatomic distances in halides and chalcogenides. Acta Crystallographica Section A, 32, 751–767.

Shaw, D.B. and Weaver, C.E. (1965) The mineralogical composition of shales. Journal of Sedimentary Research, 35, 213–222.

Shawe, D.R. (2011) Uranium-vanadium deposits of the Slick Rock district, Colorado, Professional Paper 576-F, 80. U.S. Geological Survey.

Simandl, G.J. and Paradis, S. (2022) Vanadium as a critical material: Economic geology with emphasis on market and the main deposit types. Applied Earth Science, 131, 218–236.

Simandl, G.J., Paradis, S., and Simandl, L. (2023) Future of photovoltaic materials with emphasis on resource availability, economic geology, criticality, and market size/growth. CIM Journal, 1–25.

Slack, J.F., Falck, H., Kelley, K.D., and Xue, G.G. (2016) Geochemistry of host rocks in the Howards Pass district, Yukon-Northwest Territories, Canada: Implications for sedimentary environments of Zn-Pb and phosphate mineralization. Mineralium Deposita, 52, 565–593.

Środoń, J., Elsass, F., McHardy, W.J., and Morgan, D.J. (1992) Chemistry of illite-smectite inferred from TEM measurements of fundamental particles. Clay Minerals, 27, 137–158.

Su, Y., and Hu, D. (2022) Global Dynamics and Reflections on Critical Minerals. E3S Web of Conferences, 352.

Tribovillard, N., Algeo, T.J., Baudin, F., and Riboulleau, A. (2012) Analysis of marine environmental conditions based on molybdenum–uranium covariation—Applications to Mesozoic paleoceanography. Chemical Geology, 324–325, 46–58.

Turner, E.C. (2010) Stratigraphy of the Mackenzie Mountains supergroup in the Wernecke Mountains, Yukon. In K.E. MacFarlane, L.H. Weston, and C. Relf, Eds., Yukon Exploration and Geology 2010, p. 207–231. Yukon Geological Survey.

Turner, E.C. and Long, D.G.F. (2008) Basin architecture and syndepositional fault activity during deposition of the Neoproterozoic Mackenzie Mountains supergroup, Northwest Territories, Canada. Canadian Journal of Earth Sciences, 45, 1159–1184.

Turner, E.C., Roots, C.F., MacNaughton, R.B., Long, D.G.F., Fischer, B.J., Gordey, S.P., Martel, E., and Pope, M.C. (2011) Stratigraphy. In E. Martel, E.C. Turner, and B.J. Fischer, Eds., Geology of the Central Mackenzie Mountains of the Northern Canadian Cordillera, Sekwi Mountain (105P), Mount Eduni (106A), and Northwestern Wrigley Lake (95M) Map-Areas, Northwest Territories, NWT Special Volume 1, p. 31–192. Northwest Territories Geological Survey.

USGS (2022) 2022 Final List of Critical Minerals. U.S. Geological Survey.

Veselovský, F., Pašava, J., Pour, O., and Ackerman, L. (2021) Origin of V-Cr-Ti-mineralization in thermally overprinted metal-rich black shales from the Teplá-Barrandian Unit (Bohemian Massif) and implications for metal remobilization during metamorphism. Journal of Geosciences, 66, 263–275.

Viljoen, M. (2016) The Bushveld Complex-Host to the world's largest platinum, chromium and vanadium resources. Episodes, 39, 238–268.

Vine, J.D. and Tourtelot, E.B. (1970) Geochemistry of black shale deposits: A summary report. Economic Geology and the Bulletin of the Society of Economic Geologists, 65, 253–272.

Vitolo, S., Seggiani, M., Filippi, S., and Brocchini, C. (2000) Recovery of vanadium from heavy oil and Orimulsion fly ashes. Hydrometallurgy, 57, 141–149.

Wanty, R.B. and Goldhaber, M.B. (1992) Thermodynamics and kinetics of reactions involving vanadium in natural systems: Accumulation of vanadium in sedimentary rocks. Geochimica et Cosmochimica Acta, 56, 1471–1483.

Wei, D., Wang, H., Feng, X., Chueh, W.-T., Ravikovitch, P., Lyubovsky, M., Li, C., Takeguchi, T., and Haller, G.L. (1999) Synthesis and characterization of vanadium-substituted mesoporous molecular sieves. The Journal of Physical Chemistry B, 103, 2113–2121.

Wenk, H.R., Huang, J., Devoe, M., Gómez-Barreiro, J., Vasin, R., Ren, Y., and Barrios-Sánchez, S. (2022) Crystallographic and shape preferred orientation producing anisotropy in slates from Northern Spain. Journal of Structural Geology, 164, 104730.

Whitney, D.L. and Evans, B.W. (2010) Abbreviations for names of rock-forming minerals. American Mineralogist, 95, 185–187.

Woodsworth, G.J., Anderson, R.G., and Armstrong, R.L. (1991) Plutonic regimes. In H. Gabrielse and C.J. Yorath, Eds., Geology of the Cordilleran Orogen in Canada, Geology of Canada, no. 4, 491–531. Geological Survey of Canada.

Yang, L., Li, Z., Ouyang, Y., Deng, T., D'ng, Y., and Xu, D. (2023) Mannardite as the main vanadium-hosting mineral in black shale-hosted vanadium deposits, South China. American Mineralogist, 109, 359–373.

Yates, D.M. and Rosenberg, P.E. (1997) Formation and stability of end-member illite: II. Solid equilibration experiments at 100 to 250 °C and $P_{v,soln}$. Geochimica et Cosmochimica Acta, 61, 3135–3144.

Zhou, M.-F., Robinson, P.T., Lesher, C.M., Keays, R.R., Zhang, C.-J., and Malpas, J. (2005) Geochemistry, petrogenesis and metallogenesis of the panzhihua gabbroic layered intrusion and associated Fe-Ti-V oxide deposits, Sichuan Province, SW China. Journal of Petrology, 46, 2253–2280.

Manuscript received November 2, 2024
Manuscript accepted July 9, 2024
Accepted manuscript online July 16, 2024
Manuscript Handled by Denis Fougerouse

Endnotes:

[1]Deposit item AM-25-39359. Online Materials are free to all readers. Go online, via the table of contents or article view, and find the tab or link for supplemental materials.